

## ABSTRACT

FEDI, FEHRI. Development and Characterization of a Hastelloy N-based ODS Alloy using Conventional Sintering and Laser Powder Bed Fusion Additive Manufacturing (under the direction of Dr. Djamel Kaoumi).

Hastelloy N was developed for the fuel-facing structural material during the Molten Salt Reactor Experiment in the 1960s at Oak Ridge National Laboratory. While it has good corrosion properties, it showed some limitations regarding radiation resistance, especially regarding swelling. In this work, we propose to develop an oxide dispersion strengthened (ODS) version of that alloy before further chemical composition alteration of the alloy matrix. This is done using custom-made Hastelloy N powder with additions of  $Y_2O_3$  powder and either Ti or Zr powders. Two routes have been envisioned: (i) mechanical cryo-milling of the powders followed by cold-pressing and sintering and (ii) laser powder bed fusion additive manufacturing of the powders. Microstructural characterization of the samples is then conducted using transmission electron microscopy (TEM) with energy dispersive x-ray spectroscopy (EDS). The oxide particle size distribution, number density, and volumetric density are estimated for the different samples. A discussion is conducted to relate the processing routes and parameters with the observed microstructure including the oxide size distribution,

© Copyright 2022 by Fedi Fehri

All Rights Reserved

Development and Characterization of a Hastelloy N-based ODS Alloy using Conventional Sintering and Laser Powder Bed Fusion Additive Manufacturing

by

Fedi Fehri

A thesis submitted to the Graduate Faculty of

North Carolina State University

in partial fulfillment of the

requirements for the degree of

Master of Science

in Nuclear Engineering

Raleigh, North Carolina

2022

APPROVED BY:

---

Djamel Kaoumi

---

Tim Horn

---

Benjamin Beeler

## **DEDICATION**

To my parents Lotfi and Hekmat, my brother Hakim, my sister Karama and my nephews Karim and Chahine. To my friends and colleagues Matthew DeJong, Philip Alarcon Furman, and Fuyun Tsai.

## **BIOGRAPHY**

My name is Fedi Fehri. I was born in Tunisia; I have an engineering degree in materials science from the National School of Engineering of Sfax, Tunisia. I have pursued a MS degree in Nuclear Engineering at North Carolina State University. I decided to pursue this degree to enrich my knowledge and experience characterizing superalloys made for extreme conditions. At NC State, I got the chance to gain this knowledge by joining Dr.Kaoumi's Nuclear Materials group.

## ACKNOWLEDGMENTS

First, I want to thank my parents and siblings for their unconditional support and love; I wouldn't be the person I'm today without them.

I want to thank all my colleagues in my research group for being my close friends and for making my stay at NC State much easier, and Dr. Kaoumi for giving me this opportunity to work as a research assistant on a project that I am passionate about and for his guidance and supervision. I want to thank Dr. Horn and Sourabh Saptarshi for their help consolidating the samples and making the equipment in CAMAL available for use. I want to thank Dr. Hosemann of the University of California, Berkeley for providing us with the sintered samples and the cryo-milled powder.

I want to thank Matthew DeJong for conducting some of the FIB and TEM characterization and being a supportive friend. Fu-yun Tsai for being a helpful colleague. Lucia Rebecca Hurtado Gomez and Dr Angelica Morales for helping with conducting some TEM and FIB experiments.

I would like to acknowledge the contributions of our collaborators, Dr. Armstrong and Dr. Gardner from the University of Oxford and Dr. Ryan Schoell from Sandia National Laboratories.

This work was funded by the DOE NEUP award on “**Ni-based ODS alloys for Molten Salt Reactors**”. This work was performed in part at the Analytical Instrumentation Facility (AIF) at North Carolina State University, which is supported by the State of North Carolina and the National Science Foundation (award number ECCS-2025064). The AIF is a member of the North Carolina Research Triangle Nanotechnology Network (RTNN), a site in the National Nanotechnology Coordinated Infrastructure (NNCI).

## TABLE OF CONTENTS

<b>LIST OF FIGURES .....</b>	<b>vii</b>
<b>LIST OF TABLES .....</b>	<b>ix</b>
<b>Introduction: .....</b>	<b>1</b>
<b>Chapter 1 .....</b>	<b>3</b>
<b>I. Hastelloy N as a candidate structural material for the molten salt reactor.....</b>	<b>3</b>
<i>I.1. The molten salt reactor experiment .....</i>	<i>3</i>
<i>I.2. Hastelloy N microstructure description .....</i>	<i>4</i>
<i>I.3 Mechanical alloying for processing of ODS alloys.....</i>	<i>6</i>
I.3.1 Description of the Mechanical Alloying (MA) process .....	6
I.3.2 Mechanical alloying of powders for Ni based ODS in the literature .....	8
I.3.3 Optimization of the milling speed .....	9
I.3.4 Optimization of the milling time .....	10
<b>Chapter 2: Materials and Methods .....</b>	<b>15</b>
<b>I. Materials.....</b>	<b>15</b>
<i>I.1. Powder composition .....</i>	<i>15</i>
<b>II. Powder characterization .....</b>	<b>16</b>
<i>II.1 Hastelloy N powder.....</i>	<i>16</i>
II.1.1 Powder morphology and size distribution.....	16
II.2.2 Transmission electron microscopy.....	16
<b>III. Powder milling.....</b>	<b>17</b>
<i>III.1 UCB milled powder.....</i>	<i>19</i>
<i>III.2. Summary on Powder morphology and size distribution.....</i>	<i>21</i>
<i>III.3. Summary of Powder microstructure characterization.....</i>	<i>23</i>
<b>IV. Consolidation of the powders through cold pressing followed by sintering .....</b>	<b>25</b>
<b>V. Additive manufacturing .....</b>	<b>25</b>
<b>VI. Pycnometer density measurements.....</b>	<b>27</b>
<b>Chapter 3: Results.....</b>	<b>28</b>
<b>I. Hastelloy N Sintered samples.....</b>	<b>28</b>
<i>I.1 General description of the microstructure of the sintered samples.....</i>	<i>28</i>

I.1.1 UCB mechanically alloyed powder cold-pressed at 2200 psi sintered at 1125°C for 2h M2 sample characterization .....	28
I.1.2 Cryo A 1500 psi 1125°C for 2h sample (M3).....	30
I.1.3 Cryo A 2100 psi 1200C for 2h sample (M4).....	31
I.1.4 Cryo A 2200 psi 1125C for 6h sample (M5).....	33
I.1.5 Cryo B sample M6 description.....	34
I.2 Oxide size measurements.....	35
I.2.1 Oxide particle characterization of M2 House sample .....	36
<b>II. Hastelloy N additive manufactured samples .....</b>	<b>39</b>
II.1 Density measurements.....	39
II.1.1 Microstructural characterization of the LPBF samples.....	40
a) TEM characterization of sample P3.....	40
b) TEM characterization of samples P6 and P4.....	42
d) TEM characterization of sample P12 and P10 .....	46
II.2 Oxide size measurement .....	49
II.2.1 Oxide size measurements .....	49
II.2.2 Oxide particle characterization.....	51
<b>II.3 Mechanical properties of the sintered samples .....</b>	<b>53</b>
<b>Chapter 4: Discussion .....</b>	<b>54</b>
<b>I. Oxide particles characterization and size distribution .....</b>	<b>54</b>
<b>II. Effect of the sintering parameters .....</b>	<b>57</b>
<b>III. LPBF samples characterization.....</b>	<b>61</b>
III.1 Samples density and effect of the powder .....	61
III.2 Oxide size measurement of LPBF samples .....	62
III.5 Comparison between LPBF and sintering.....	64
<b>Summary and Conclusions .....</b>	<b>65</b>
<b>References .....</b>	<b>67</b>

## LIST OF FIGURES

Figure 1.1: Schematic representation of the molten salt reactor experiment [1].	4
Figure 1.2: Optical micrographs showing the general microstructure of Hastelloy N with nominal composition (A) and low silicon (B) [7].	5
Figure 1.3: Comparison of time necessary to reach a steady state in a planetary ball mill compared to attrition milling [4].	7
Figure 1.4: Microstructure of Alloy 617–0.6 Wt.% Y <sub>2</sub> O <sub>3</sub> ball milled powders at different rpm (a–d) SE micrographs of Alloy 617–0.6 Wt.% Y <sub>2</sub> O <sub>3</sub> ball milled powder at 500, 1000, 1500 and 2000 rpm respectively for 30 min showing flaky morphology at 500, flaky and convoluted at 1000, convoluted without any flakes at 1500 and 2000 [13] 2 hours of milling and 4nm after 4 hours of milling.	11
Figure 2.1: SEM picture of one powder particle showing the spherical morphology (left) and particle size distribution of the different samples: a) number size distribution and b) volume size distribution of Pure Hastelloy N powder (as received).	16
Figure 2.2: STEM-EDS maps of the Hastelloy N powder.	17
Figure 2.3: Photograph showing the Retsch PM 100 planetary ball mill.	18
Figure 2.4: SEM picture of the mechanically alloyed powder showing irregular powder shape and small size.	18
Figure 2.5: STEM-EDS map of the ball milled powder.	19
Figure 2.6: Cryo-milling machine.	20
Figure 2.7: SEM picture of the mechanically alloyed powder showing irregular powder shape and small size.	20
Figure 2.8: Powder size distribution and morphology: Secondary electron picture of a) pure Hastelloy N b) Cryo A c) Cryo B d) ball milled powder. Number size distribution of e) pure Hastelloy N f) Cryo A g) Cryo B h) ball milled powder. Volume size distribution of i) pure Hastelloy N j) Cryo A k) Cryo B l) ball milled powder.	21
Figure 2.9: TEM picture of a) pure Hastelloy n powder, b) Cryo A powder. Selected area diffraction patterns of c) powder showing a [112] zone axis typical of a nickel alloy, d) Cryo A powder.	23
Figure 2.10: Top: STEM-EDS maps of the Cryo A samples, bottom: STEM-EDS maps of the Cryo B samples.	24
Figure 2.11: Picture of the Quantachrome Ultrapyc 1200e.	27
Figure 3.1: TEM image of the Sample M2	29
Figure 3.2: STEM-EDS maps of the house sample M2.	30
Figure 3.3: TEM of M3 sample.	31
Figure 3.4: STEM-EDS chemical maps of M3 sample.	31
Figure 3.5: TEM pictures of M4 sample.	32
Figure 3.6: STEM-EDS chemical maps of M4 sample	32
Figure 3.7: TEM of sample M5.	33
Figure 3.8: STEM-EDS chemical maps of M5 sample	33
Figure 3.9: TEM of M6 sample.	34

Figure 3.10: STEM-EDS chemical maps of the Cryo B M6. ....	34
Figure 3.11: Oxide measurements for M2 sample.....	37
Figure 3.12: Oxide measurements for M3, Cryo A 1500 psi 1125°C for 2h.....	37
Figure 3.13: Oxide measurements for M4 Cryo A 2100 psi 1200°C for 2h. ....	38
Figure 3.14: Oxide measurements for the M5, Cryo A 2200 psi 1125°C for 6h.....	38
Figure 3.15: Oxide measurements for the M6 sample Cryo B 2200 psi 1150°C for 2 hours.....	38
Figure 3.16: Photograph showing the Hastelloy N samples fabricated by LPBF.....	39
Figure 3.17: TEM images of Hastelloy N P3 Sample.....	41
Figure 3.18: STEM-EDS maps of P3 sample showing Ni, Cr, Fe, Ti, O, Y. ....	41
Figure 3.19: TEM images of sample P6 sample.....	42
Figure 3.20: STEM-EDS maps of sample P6. ....	42
Figure 3.21: TEM pictures of sample P4. ....	43
Figure 3.22: STEM-EDS pictures of sample P4.....	43
Figure 3.23: TEM picture of sample P9.....	44
Figure 3.24: STEM-EDS maps of sample P9.....	45
Figure 3.25: TEM picture of P7.....	45
Figure 3.26: STEM-EDS maps of P7.....	46
Figure 3.27: TEM images of sample P12.....	47
Figure 3.28: STEM-EDS images of sample P12. ....	47
Figure 3.29: TEM pictures of P10 samples. ....	48
Figure 3.30: STEM-EDS pictures of P10 samples.....	48
Figure 4.1: Selected area diffraction of M5 sample showing a potential $Y_6ZrO_{11}$ and a $Y_4Zr_3O_{12}$ .....	56
Figure 4.2: TEM pictures of a,b) M3 Sample, c,d) M4 sample, and e,f) M5 sample.....	57
Figure 4.3: Grain size distribution: a) M3 sample, b) M4 sample, and c) M5 samples.....	58
Figure 4.4: STEM-EDS map of the different consolidated samples made from the Cryo A powder.....	59
Figure 4.5: STEM-EDS images of column a) P3 b) P6 c)P9 d)P12.....	63

## LIST OF TABLES

Table 1.1: Nominal composition of Hastelloy N.....	4
Table 1.2: Summary of the different parameters used in the literature to mechanically alloy powders for Ni based ODS alloys.....	8
Table 1.3: Summary of precipitated particles in austenitic oxide dispersion strengthening alloys[37]. .....	14
Table 2.1: Hastelloy N powder composition. ....	15
Table 2.2: Laser granulometry measurement of the different powders .....	22
Table 2.3: shows the conditions used in the process. ....	25
Table 2.4: Additively manufacturing of Hastelloy N samples with different parameters and composition.....	26
Table 3.1: Parameters used to consolidate the sintered samples. ....	28
Table 3.2: Particle size distribution. ....	35
Table 3.3: LPBF parameters used for the AM printing of the samples .....	40
Table 3.4: Oxide size measurement for the additive manufactured P-samples .....	49
Table 3.5: Hardness of the sintered samples.....	53
Table 4.1: size distribution of the oxides made from the Cryo A samples. ....	55
Table 4.2: SAED of an oxide from the M5 sample indexation results. ....	56
Table 4.3: Grain size of the different samples .....	58
Table 4.4: Density of the different samples .....	62
Table 4.5: oxide size measurement and distribution.....	64
Table 4.6: Comparison of Cryo B AM samples and Cryo B sintered sample.....	64

## **Introduction:**

Molten salt reactors (MSR) are one of the most promising generation IV designs because of their safety, reliability, and high efficiency. The reactor design started in 1960 and reached criticality in 1965 by the oak ridge national laboratory (ORNL). Materials in the molten salt reactor are subjected to severe environmental factors, such as high temperature, high neutron irradiation, and molten salts. Hastelloy N is a solid-solution nickel-based alloy (Ni- 16Mo- 7Cr- 4Fe) that was chosen as a promising structural material for molten salt reactors due to its molten salt corrosion resistance and mechanical properties.

Nevertheless, during MSR operation, neutron irradiation can still result in microstructural evolution of Hastelloy N due to the creation of defects, which can cause the degradation of mechanical properties of Hastelloy N over time. In particular,  $(n, \alpha)$  transmutation reactions result in the production of helium (He) atoms that accumulate as nanoscale bubbles in the microstructure resulting in the irradiation-induced Helium (He) embrittlement. Hastelloy N exhibited a significant amount of swelling and embrittlement[1]. Because of the small size of the He atom and its low solubility, the He bubbles tend to accumulate in defects in the crystal structure, such as voids, vacancies, stacking faults, and dislocations. A homogenous distribution of nano-scale dispersoids can act as sinks for He and therefore distribute and minimize the swelling and embrittlement effects of point defects created from irradiation damage [2,3].

Oxide dispersion strengthened (ODS) alloys incorporate nanoparticles dispersed into their matrix. These oxides not only provide sinks for radiation induced damage but also high strength and structural stability at elevated temperatures due to their ability to pin dislocations and grain boundaries[2,4]. Thus, they are widely used in high-temperature applications such as heat exchangers and nuclear power plants[3,5].

For structural applications in MSRs, an ideal material would combine the irradiation resistance of ODS with the molten salt corrosion resistance of Hastelloy N. However, to date, very little data are reported on the subject in part because of processing challenges associated with incorporating oxides into the Hastelloy N matrix. This thesis seeks to explore processing methods for producing an ODS Hastelloy N alloy including methods for incorporating oxides into precursor powders and methods for powder consolidation such as conventional sintering or laser powder bed fusion (LPBF) additive manufacturing (AM), and to elucidate their effects on the microstructure and properties.

## Chapter 1

### I. Hastelloy N as a candidate structural material for the molten salt reactor

#### I.1. The molten salt reactor experiment

The molten salt reactor was an

experimental molten salt-fuel reactor. It was operated for over 20000 hr for around 4 years from 1965 to 1969 at about 650°C at Oak Ridge National Laboratory (ORNL). The fuel consisted of fluoride salts circulating through a core of graphite bars and a heat exchanger. Except for the graphite bars, the structures in contact with the fuel were made of Hastelloy N, which exhibited the expected corrosion resistance to the fluoride salt. However, two significant problems were revealed during the operation. The first was a drastic drop in creep-rupture life and fracture strain under creep conditions. The second was the appearance of grain-boundary cracks at surfaces exposed to the fuel salt. This embrittlement was attributed to the formation of helium bubbles resulting from  $n,\alpha$  transmutation reactions [1].

A scheme presenting the MSR is illustrated in Figure 1.1. The fuel salt composition was  $\text{LiF-BeF}_2\text{-ZrF}_4\text{-UF}_4$ , the coolant,  $\text{LiF-BeF}_2$ . At full power, the full stream entered the reactor vessel at 632°C and leaves at 654°C; the maximum operating temperature was 663°C. The salt system was held at 650°C when the reactor was at low power. During extended shutdowns, the salt was drained into tanks where it was kept molten while the circulating loops were cooled[6].

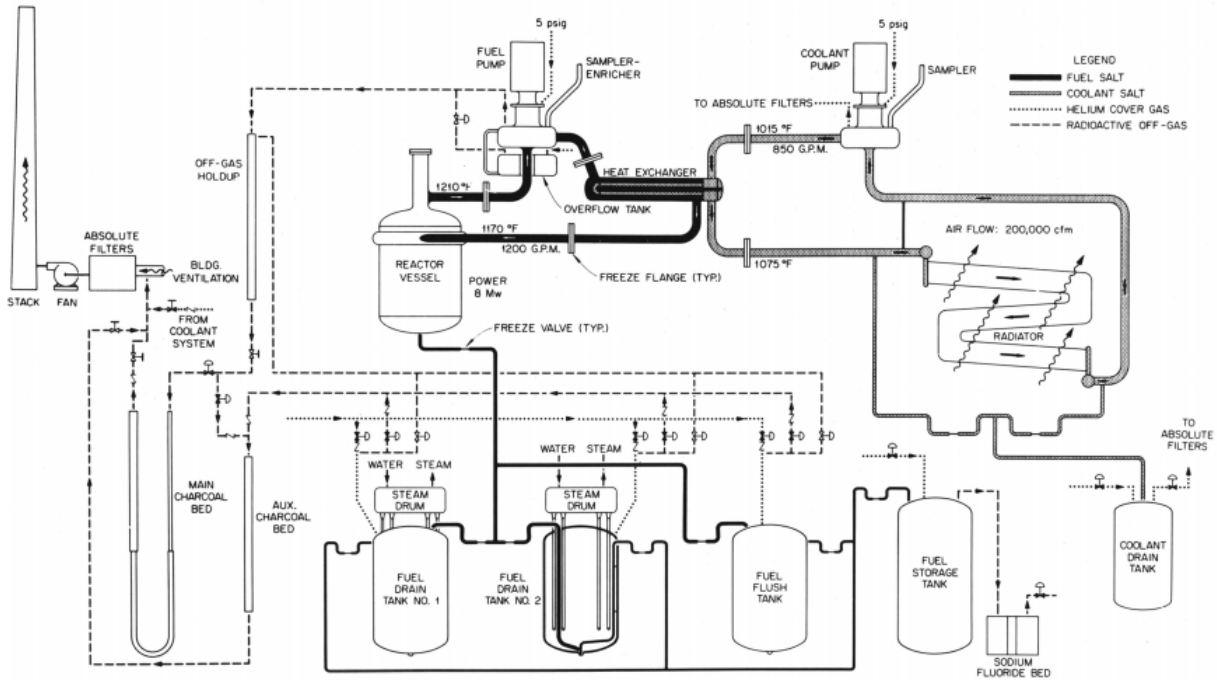


Figure 1.1: Schematic representation of the molten salt reactor experiment [1].

## I.2. Hastelloy N microstructure description

Table 1.1. shows the nominal composition of Hastelloy N.

Table 1.1: Nominal composition of Hastelloy N.

Alloy	Composition										
	Ni	Cr	Fe	Co	Mo	W	C	Mn	Si	B	Other
Hastelloy N	Bal	6.0-8.0	5.0	0.2	15.0-18.0	0.5	0.01	1.0	1.0	0.10	0.5V, 0.35Cu

An example of the microstructure of Hastelloy N is shown in Figure 1.2. The alloy has an FCC crystal structure and shows large  $M_6C$ -type (typically  $Ni_3Mo_3C$  [7] or  $Ni_2Mo_4C$  [8]) inclusions heterogeneously distributed along grain boundaries in stringers aligned with the rolling direction. These precipitates are formed during casting and remain after annealing and rolling.

The size and number of these particles is found to vary inversely with silicon content, with higher concentrations of silicon resulting in smaller the lattice parameter and reduced size. Other carbides can also form during annealing in the alloy. In air-melted heats containing 0.6 wt% Si or more, the carbides are enriched in silicon. The only carbides that form in air at a high temperature of 1180°C are pseudo-carbides with complex compositions dependent on the silicon content such as  $\text{Ni}_3(\text{Mo}, \text{Cr})_3(\text{C}, \text{Si})$  and  $\text{Ni}_2(\text{Mo}, \text{Cr})_4(\text{C}, \text{Si})$  types. Silicon is found to stabilize particles and prevents them from dissolving into the solid solution at high annealing temperatures. When such carbides form, the matrix can be locally depleted in Mo and Si. Grain boundary precipitates form in the temperature range of 500°C to 700°C and have a fine dendritic morphology.

According to Gao et al., the average grain size of a commercial Hastelloy N provided by Haynes should be around 80  $\mu\text{m}$ [9], but it can be further reduced to 10  $\mu\text{m}$  with a pre-strain of 10%. Grain size increases with the increase of annealing temperature and duration [7]. Si content is also found to affect the grain size as shown in Figure 1.2. with lower Si content resulting in smaller grain size.

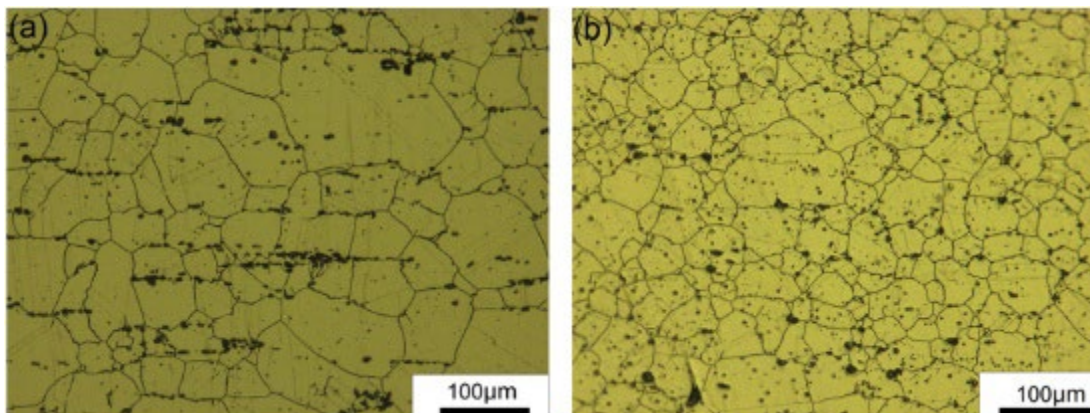


Figure 1.2: Optical micrographs showing the general microstructure of Hastelloy N with nominal composition (A) and low silicon (B) [7].

### **I.3 Mechanical alloying for processing of ODS alloys**

ODS alloys are typically manufactured by mechanical alloying (MA) precursor powders that are then consolidated by solid-state methods like sintering spark plasma sintering (SPS) [10–12] hot isostatic pressing (HIP) [13,14] or hot extrusion[15]. The pre-alloyed powders are usually mechanically alloyed with  $Y_2O_3$  particles using a planetary mill to form a solid solution. The ball-to-powder ratio is usually around 10:1 [16–18]. The alloying process is usually made in an inert gas atmosphere to avoid contamination [19].

#### **I.3.1 Description of the Mechanical Alloying (MA) process**

Many variables must be controlled during Mechanical Alloying, such as the ball-to-powder ratio (BPR), ball size, atmosphere, and milling speed. The milling atmosphere is usually an inert gas like Ar. There are several types of mills. The SPEX shaker mills, planetary ball mills, and attritor mills are the most common [10]. Figure 1.3 shows how the time required to reach steady state particle size in an attritor mill is much faster than in a planetary ball mill.

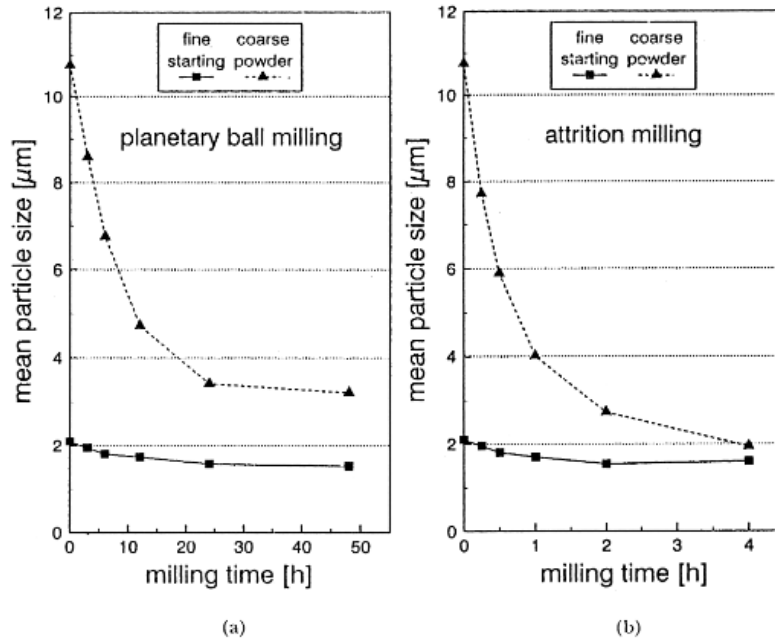


Figure 1.3: Comparison of time necessary to reach a steady state in a planetary ball mill compared to attrition milling [4].

The process variables are crucial to obtaining the desired particle size. The milling time is one of the most important parameters. Excessive milling time can lead to contamination from wear products (from the steel balls or jar). This, in turn can result in the formation of undesirable phases. The milling time should be optimized to achieve a steady state balance between the fracturing and cold welding of the particles. The grinding medium (the balls) is generally made from hardened steel, tool steel, hardened chromium steel, tempered steel, stainless steel, WC-Co, or bearing steel. It is desirable for the grinding medium and the grinding vessel to be made of the same material. The combination of balls of different sizes can be beneficial for better mixing [19].

Energy transferred to the powder from the balls during milling is proportional to the square of the speed of the process. However, certain high-speed limitations exist depending on the mill's design and the vial/jar form. For example, at rotational speeds above some critical value the centrifugal force causes the balls to stick to the walls of the jar reducing the interaction between

the balls and the powder. Another inconvenience is that high speed in some cases could lead to the decomposition of supersaturated solid solutions due to the increase in temperature [13]. Since alloying occurs due to collision forces, there must be enough space for the ball and the powder to move freely and interact.; 50% to 66% of the vial must be empty according to Retsch website[20].

### I.3.2 Mechanical alloying of powders for Ni based ODS in the literature

Table 1.2 summarizes typical parameters used to mechanically alloy powders for processing Ni based ODS alloys in the literature. From this table it is shown that the tendency is to mill the powder for long duration > 4 hours or at high speed > 200 rpm for samples milled using a planetary ball mill.

Table 1.2: Summary of the different parameters used in the literature to mechanically alloy powders for Ni based ODS alloys.

Powder	Process	BPR	Ball size (diameter) and material	Time and rotation speed	Reference
Ni-TiC	Planetary milling	10:1	10mm stainless steel	Disc 600rpm and vial 320rpm	[21]
Ni-15Cr-4.5Al-4W- 2.5Ti-2Mo-2Ta- 0.15Zr-1.1 Y <sub>2</sub> O <sub>3</sub>	Horizontal ball milling	15:1	N/A	1 to 5 hr 4min at 1200 rpm followed by 1 min at 900 rpm	[22]
Ni-22.3Cr-0.1Fe 12.7Co-8.70Mo-0.6Ti- 0.6Al - 0.30Si-0.6 Y <sub>2</sub> O <sub>3</sub>	Planetary ball milling	15:1	N/A	14 hr at 200 rpm	[23]
617 ODS alloy	Planetary ball milling	10:1	5mm stainless steel	Varying from 500 to 2000 rpm	[18]
ODS NiCr20 0.5Y <sub>2</sub> O <sub>3</sub>	Planetary ball milling	10:1	8mm steel	600 rpm 24 hr (optimal)	[16]
Ni-20Cr, 1.2 Y <sub>2</sub> O <sub>3</sub> ,	Planetary ball milling	10:1	5mm stainless steel	2 hr and 4 hr	[17]
-66% Ni + 22% Cr + 11% Fe + 1% TiO <sub>2</sub>	Planetary ball milling	40:1	6.35mm martensitic stainless-steel (vial and balls)	150 rpm-20 hrs optimal	[24]

### I.3.3 Optimization of the milling speed

The milling speed is a parameter of importance affecting the ability of the mechanically alloyed powder to be effectively used for subsequent consolidation.

Calculating the energy transferred to the powder can be relevant in optimizing the different parameters. Different models for transferred energy have been proposed in the literature. The transferred energy depends on the steel balls and the mill type. In the model proposed by Magini *et al.* [25] , the energy transferred per unit of mass; per collision is given by:

$$E_c = \frac{[7.66 \times 10^{-2} \times R_D^{1.2} \times \rho^{0.6} \times E^{0.4}]d_b w_d^{1.2}}{\sigma}$$

Where:  $R_d$ : radius of supporting disk.  $\rho$  : the density of the grinding ball,  $w_d$ : Angular velocity of the disk,  $\sigma$ : surface density of the powder covering the ball.  $E$ : elastic modulus of the grinding ball.  $d_b$ : diameter of the grinding ball.

For the study by Sivakumar et al [18] where the speed was varied from 500 to 2000 rpm, the energy transferred per unit mass corresponding to angular values of 500, 1000, 1500, and 2000 rpm has been calculated as: 178.04, 409.02, 665.36, and 939.68 J/g.hit respectively. These energies are considerably higher than the transferred energy during planetary ball milling which typically is 45 J/g.hit at 270 rpm[25]. Such high energy could cause unwanted effects like cold welding and the coalescence of powder particles. Therefore, the rpm must be optimized. In [18] Different Ni-617 alloy powders were mechanically alloyed for 30min to varying values of angular rotation speeds 500, 1000,1500, and 2000 rpm, resulting in different powder morphologies. Although the powder milled at 2000 rpm exhibited a desirable morphology, the quantity of usable powder was low. This is attributed to the cold welding of the powder to the side walls of the jars and to the grinding medium, which transferred energy of 0.9 kJ/g.hit at 2000 rpm. Using stearic acid is

usually known to reduce this effect. Within the constraints of the study, a speed of 1500 rpm for a milling duration of 30 minutes was determined to be an optimum. However, a wide distribution of powder size was observed, so the authors increased the milling duration to 1 hour which resulted in a more a uniform particle size distribution that is generally favorable for consolidation.

### **I.3.4 Optimization of the milling time**

Pasebani et al. [16] studied the milling time effect in nickel-based ODS alloys. Using the following powder composition Ni-19.6Cr-0.2Fe-0.8Mn-0.9Si (wt %) and high purity  $Y_2O_3$  particles with a mean size of 30-40 nm and  $Al_2O_3$  powder with a particle size in the range of 300-400 nm and process control agent (1wt% stearic acid) was added to the milling vial t in a glove box under an argon gas atmosphere. The process was carried out in a SPEX 8000M using 5 mm in diameter steel balls and a BPR of 10:1, and A variety of Ni-based alloys altering in time (0h, 2h, and 4h). The milling speed in this article is not mentioned. After 2 hours of milling, the ductile powder transforms into flat and cold-welded powder trapping  $Y_2O_3$  between the Ni-20Cr lamellae. The morphology of the powder particles became round, and the mean size of the grains was 33.6  $\mu m$ . The deformed layers are apparent in the powder lamella after 2h of milling. The agglomeration of the powders continued even after 4h of milling. However, some cracks appeared. Essentially, the accumulation of work hardening led to fatigue which could lead to refinement upon further milling. The powder shape is round and has an average particle size of 39.4  $\mu m$ . The XRD pattern for Ni-20Cr-1.2 $Y_2O_3$  shows that the structure is FCC for the Ni-20Cr, and the remaining peaks showed a cubic form, especially  $Y_2O_3$ . The peaks broadened after 2h of milling due to refinement and disappeared completely after 2 hours.

However, the Ni-20Cr shifted to lower diffraction angles due to the partial dissolution of  $Y_2O_3$  into the matrix. The average crystallite size has constantly and highly decreased from 44 nm in the raw powder to 14 nm after 8 hours milling.

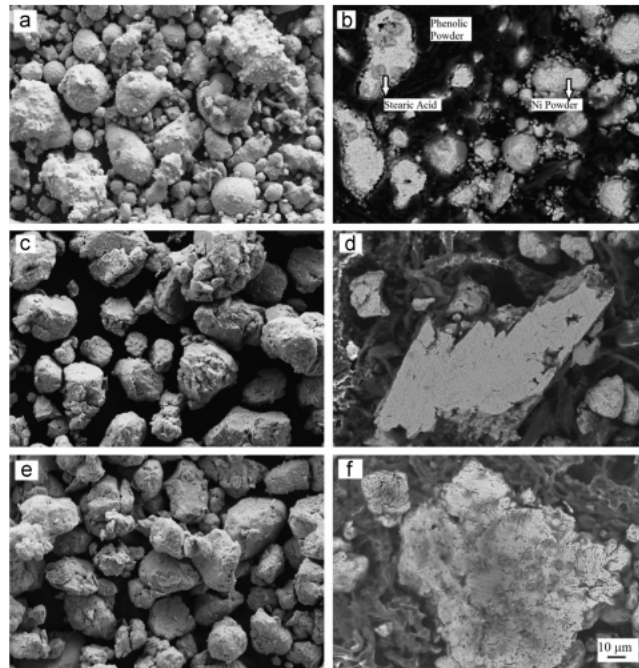


Figure 1.4: Microstructure of Alloy 617–0.6 Wt.%  $Y_2O_3$  ball milled powders at different rpm (a–d) SE micrographs of Alloy 617–0.6 Wt.%  $Y_2O_3$  ball milled powder at 500, 1000, 1500 and 2000 rpm respectively for 30 min showing flaky morphology at 500, flaky and convoluted at 1000, convoluted without any flakes at 1500 and 2000 [13] 2 hours of milling and 4nm after 4 hours of milling.

#### I.4. Microstructure of Ni-base ODS alloys

The microstructure of ODS alloys is strongly dependent on the initial powder composition as well as powder contamination during the fabrication process and the applied fabrication route. The nano-oxides that precipitated during the consolidation process can generally be represented by chemical composition:  $A_xB_yO_z$ . The elements that occupy the position A and B will depend on the initial powders elements and their affinity to oxidized. For instance, in the absence of Al, Y-Ti-O oxides such as pyrochlore  $Y_2Ti_2O_7$  and orthorhombic  $Y_2TiO_5$  are typically formed[27–30]. While in Al-added ODS alloys, the formation of  $Y_4Al_2O_9$  (YAM, monoclinic),  $YAlO_3$  (YAP, orthorhombic),  $YAlO_3$  (YAH, hexagonal) and  $Y_3Al_5O_{12}$  (YAG, cubic) are commonly reported[31]. One important feature, however, of the precipitated particles is their size and distribution within the matrix. Both parameters influence the mechanical properties of the resulting alloy. Smaller the particle size and lower the mean interparticle spacing, the better the mechanical properties of the resulting ODS alloy[31].

During the fabrication stages of ODS alloys, and especially during milling powder has also been subjected to contamination, especially by the incorporation of O, C, and N. Such contamination by impurity intake can also have a significant impact on the microstructure of the resulting ODS alloys. Incorporation of C and N has been found to promote the formation of undesirable carbides and nitrides; while large incorporation of oxygen in excess can influence the microstructure of the resulting ODS alloys by favoring the formation of some types of oxides particles over other ones. These promoted changes in the microstructure of the product by the intaking impurity content will naturally affect the mechanical properties of the resulting ODS alloys. For instance, in 9Cr-ODS steels, a special group of ODS steel which have been extensively studied, an excess intaking of oxygen content as well as titanium percent decreases have been found to negatively impact the hardness of steels and the tempering-induced-softening[32]. The microstructure of the extruded 9Cr-ODS steel containing low excess of oxygen typically consisted of a mixture of elongated grain and equiaxed grain, while for alloys containing high excess of oxygen the microstructure was composed of only uniformed equiaxed grain[32]. The elongated grain was found to has ultra-fine oxide particle distribution and higher hardness; while, equiaxed grain has relatively larger oxide particle distribution[32]. However, it is important also to point out that too low oxygen addition might also affect the mechanical properties of the ODS alloys by

preventing the formation of the nano-oxide particles or resulting in a lower volume fraction of the dispersoids. Besides, lack of oxygen might also favor the formation of undesirable precipitates as can be titanium carbide instead of titanium oxide in C containing ODS alloys[32]. This suggests that the oxygen intaking by the powder should be carefully controlled.

In regard of how the processing route of Ni-ODS alloys affect the microstructure of the resulting product, it has been established that powder subjected to hot-extrusion or hot rolled materials exhibit elongated grains and a textured microstructure, although the direction of grain growth in hot-extruded Ni-ODS powder can be relatively controlled by the temperature gradient during zone annealing[33]. On the other hand, powder consolidated by HIP or SPS usually contains spherical grains without texture.

The typical reported grain size of Ni-ODS alloys is generally smaller compared to their conventional alloy counterpart. For instance, the average grain size of 617-ODS alloys produce through BM and consolidate through HIP was found to be 1 $\mu$ m in diameter, while in the conventional 617 alloys the average grain size was determined as 30  $\mu$ m[34]. Many researchers believe that this refinement of the grain size is attributed to the mechanical alloying process, although the pinning force that the nano-oxides exert in the walls of the grains that grow during the recrystallization of the metal also play a role. Typical values of grain size of consolidated powder found in the literature for austenitic ODS alloys vary from 200 nm to 1  $\mu$ m[34,35].

The size of the nano-oxides generally varies from 2 nm to 100 nm [31,34,35]. Addition of transition elements such as Ti, Zr, and Hf have been found to effectively propitiate the formation of oxide particles that are smaller in size, higher in number density, and with smaller interparticle spacing[30,31,36]. On the other hand, the temperature of heat treatment has also been established to influence dispersoid size and interspacing. In a work performed by Man Wang et al. [36]and increases of heat treatment temperature for 890 to 1014°C of the as-MA powder composition Ni–30Cr–11Fe–0.50Ti–1.36Gd<sub>2</sub>O<sub>3</sub> was found to favor the refinement of the precipitated oxide particles as well their inter-spacing.

In general remarks, it could be said that several kinds of dispersoid might form in austenitic ODS alloys. A summary of their chemical formula and principal characteristics is present in Table 1.3. All of these types of oxides can exhibit different orientation relationships with the matrix, which is related to crystal structure and particle size. For dispersoids with the same crystal structure, the interface structure is greatly dependent on particle size and the coherency tends to lose for dispersoids with large size due to the increased strain energy.

Table 1.3: Summary of precipitated particles in austenitic oxide dispersion strengthening alloys[37].

Clusters	Morphology	Crystal structure	Size (nm)
TiN	Polyhedral	Sodium chloride	100
YAH	spherical	Hexagonal	20-80
YAP	spherical	Perovskite	20-80
Y <sub>2</sub> Ti <sub>2</sub> O <sub>7</sub>	-	pyrochlore	<10
Y <sub>2</sub> TiO <sub>5</sub>	-	orthorhombic	<10
Y <sub>2</sub> O <sub>3</sub>	spherical	cubic	30
Y <sub>2</sub> Hf <sub>2</sub> O <sub>7</sub>	Faceted	Pyrochlore	<10
Y <sub>2</sub> Zr <sub>2</sub> O <sub>7</sub>	hexagonal	Pyrochlore	<10
YAM	spherical	Monoclinic	20
YAG	spherical	Cubic	20
Y <sub>2</sub> Si <sub>2</sub> O <sub>7</sub>	rectangular	Monoclinic	<400
TiO	spherical	HCP	<400

## Chapter 2: Materials and Methods

In this chapter the different materials and characterization methods are presented,

### I. Materials

#### I.1. Powder composition

The Hastelloy N powder used in this study was manufactured by Haynes international and the composition is provided in Table 2.1. Also provided in Table 2.1 are the compositions of the cryo-milled powders described in more details later.

Table 2.1: Hastelloy N powder composition.

Composition wt. %											
Alloy	<i>Ni</i>	<i>Cr</i>	<i>Fe</i>	<i>Co</i>	<i>Mo</i>	<i>W</i>	<i>Cu</i>	<i>C</i>	<i>Mn</i>	<i>Si</i>	<i>Other</i>
<b>Hastelloy N powder (As received)</b>	Bal	7.3	3.3	0.06	15.9	0.01	0.05	0.06	0.1	1.0	0.5V +0.015S+0.015P
<b>Hastelloy N powder Cryo-milled (Batch B)</b>	Bal	7	4		16						0.5Zr+0.7 Y <sub>2</sub> O <sub>3</sub>
<b>Hastelloy N powder Cryo-milled (Batch B)</b>	Bal	7	4		16						0.5Ti + 0.7 Y <sub>2</sub> O <sub>3</sub>

## II. Powder characterization

### II.1 Hastelloy N powder

#### II.1.1 Powder morphology and size distribution

Figure 2.1 shows an SEM picture of a single particle of Hastelloy N powder with a typical, spherical morphology.

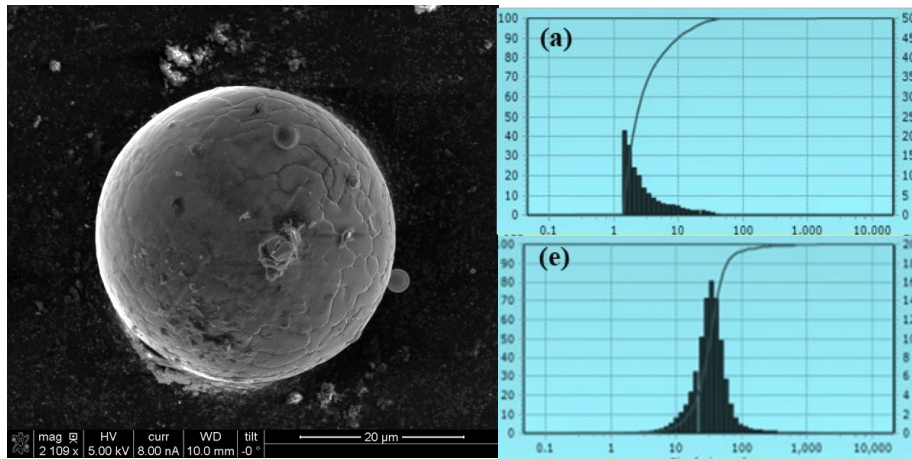


Figure 2.1: SEM picture of one powder particle showing the spherical morphology (left) and particle size distribution of the different samples: a) number size distribution and b) volume size distribution of Pure Hastelloy N powder (as received) .

#### II.2.2 Transmission electron microscopy

TEM characterization was done of the Hastelloy N powder and is shown in Figure 2.2. Particularly the STEM-EDS maps show a rather homogeneous matrix (solid solution).

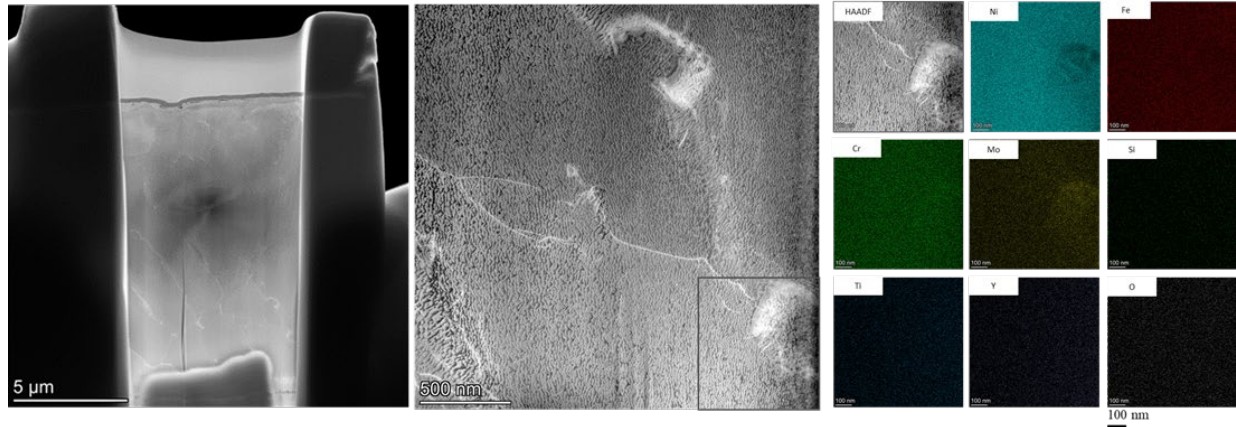


Figure 2.2: STEM-EDS maps of the Hastelloy N powder.

### III. Powder milling

The Hastelloy N powder was milled with additional  $Y_2O_3$  and Ti or Zr powders either (i) at NCSU using a planetary mill (2) or at UCB using in house milling or cryo-genic milling (through a third party: Nanotechnologies Inc company).

#### III.1 Powder milled at NCSU

A Retsch PM100 planetary ball mill was used. A photograph of the unit is shown in Figure 2.3. 12-mm diameter stainless steel balls were used as the grinding media. The first powder batch was milled for 24 hours at 300 rpm with a ball-to-powder ratio of 4:1. The powder mix consisted of Hastelloy N powder with 2%wt Ti and 2%wt  $Y_2O_3$  was prepared and poured into the planetary ball milling machine jar inside a glove box with a protective gas environment of argon (<1% vol oxygen). The balls were 12 mm in diameter stainless steel balls. The milling was performed with the addition of 2% of stearic acid as a process control agent.

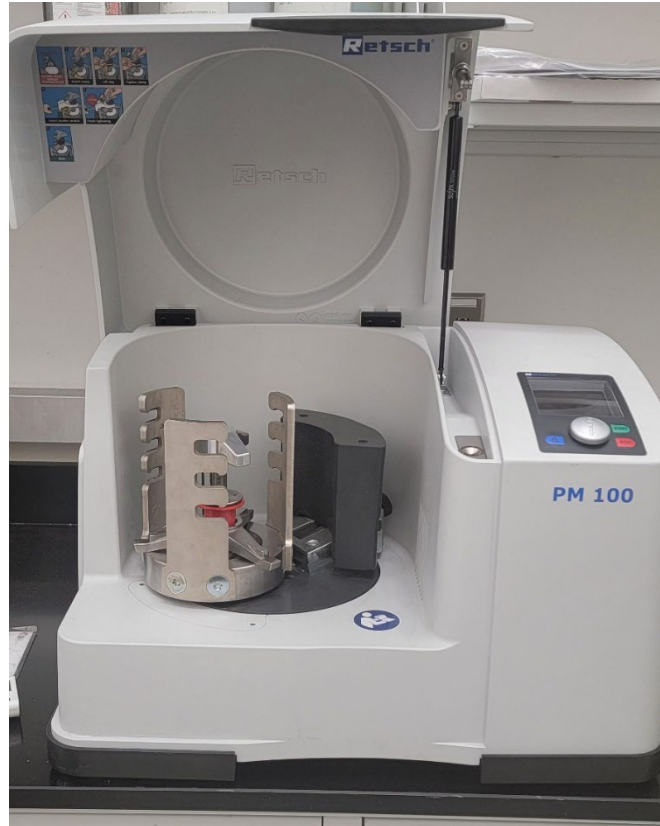


Figure 2.3: Photograph showing the Retsch PM 100 planetary ball mill.

A SEM picture of the mechanically alloyed powders is shown in Figure 2.4.

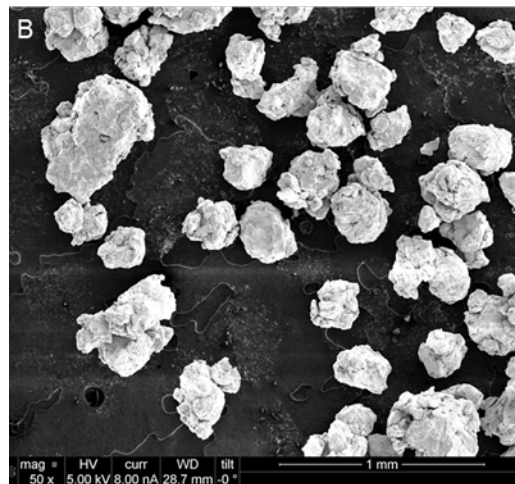


Figure 2.4: SEM picture of the mechanically alloyed powder showing irregular powder shape and small size.

Figure 2.5 present a different region of the Hastelloy N powder that was ball milled. The STEM maps are shown below, emphasizing other areas concentrated in Yttrium.

The STEM-EDS maps of a yttrium particle show that it's slightly rich in oxygen. Yttrium oxide concentration seems low as only one particle is displayed, which appears much bigger than desired.

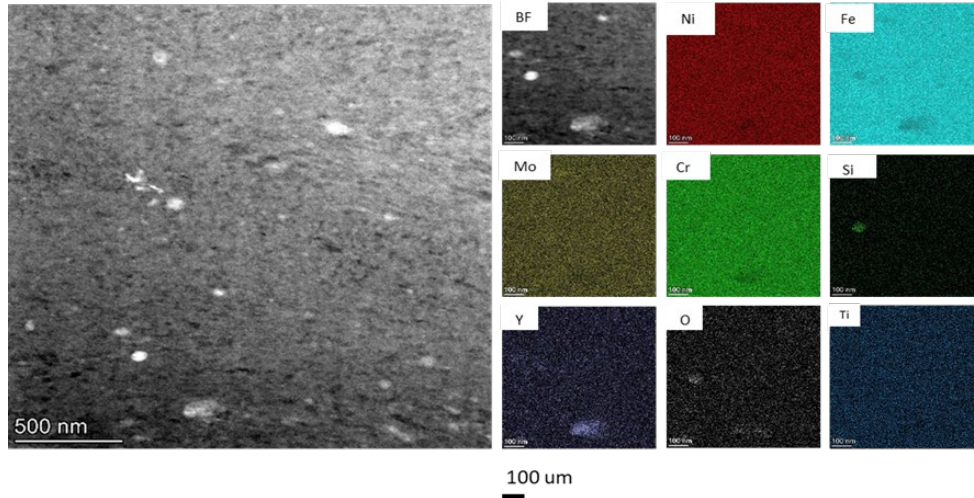


Figure 2.5: STEM-EDS map of the ball milled powder.

### III.1 UCB milled powder

Two batches of powder described as cryo-A and cryo-B powders prepared by cry-milling and provided by University of California-Berkeley. Batch A had a composition of 98.8% Hastelloy N, 0.5%Zr, and 0.7%  $Y_2O_3$ , and batch B had a composition of 98.8% Hastelloy N and 0.5%Ti and 0.7%  $Y_2O_3$ . They were milled for 8 hrs at 180 rpm with 6.35 mm stainless steel grinding balls by Nanotechnologies Inc (for the University of California-Berkeley). The cryo-milling process was conducted under liquid nitrogen to prevent cold welding of the powders. This route was chosen because of the poor yield of preliminary run due to the cold welding to the walls of the jars. Figure 2.6 shows the cryo-milling machine.



Figure 2.6: Cryo-milling machine.

Figure 2.7 shows the morphology of the cryo-milled powder, which shows a flaky morphology. Also noticeable is the effect of the milling route on the size of the powder with the ball milled powder being way smaller than the cryo-milled powder (for the milling parameters used in this study).

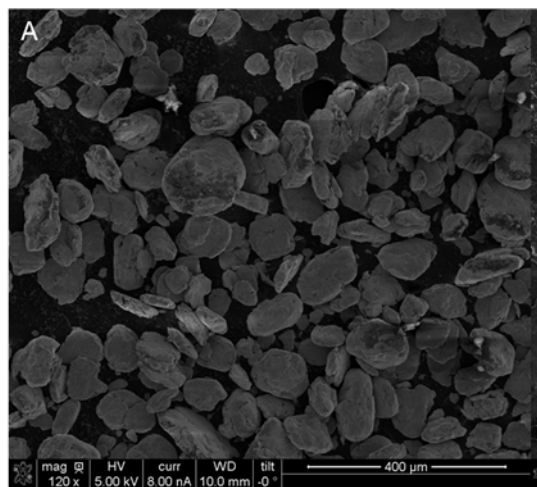


Figure 2.7: SEM picture of the mechanically alloyed powder showing irregular powder shape and small size.

### III.2. Summary on Powder morphology and size distribution

Figure 2.8 shows the morphology of all powders. Typically pure Hastelloy N powder—showed a spherical morphology. The number size distribution and the volumetric size distribution of each powder are shown in Figures 2.8.d and 2.8.g, respectively. Table 2.2 summarizes the results obtained, showing the 10th, 50th, and 90th percentile of the volumetric distribution and the number distribution. Note that the ideal size that provides a good powder flow is in the range of 15-45  $\mu\text{m}$ . However, the powder for pure Hastelloy N has good flowability.

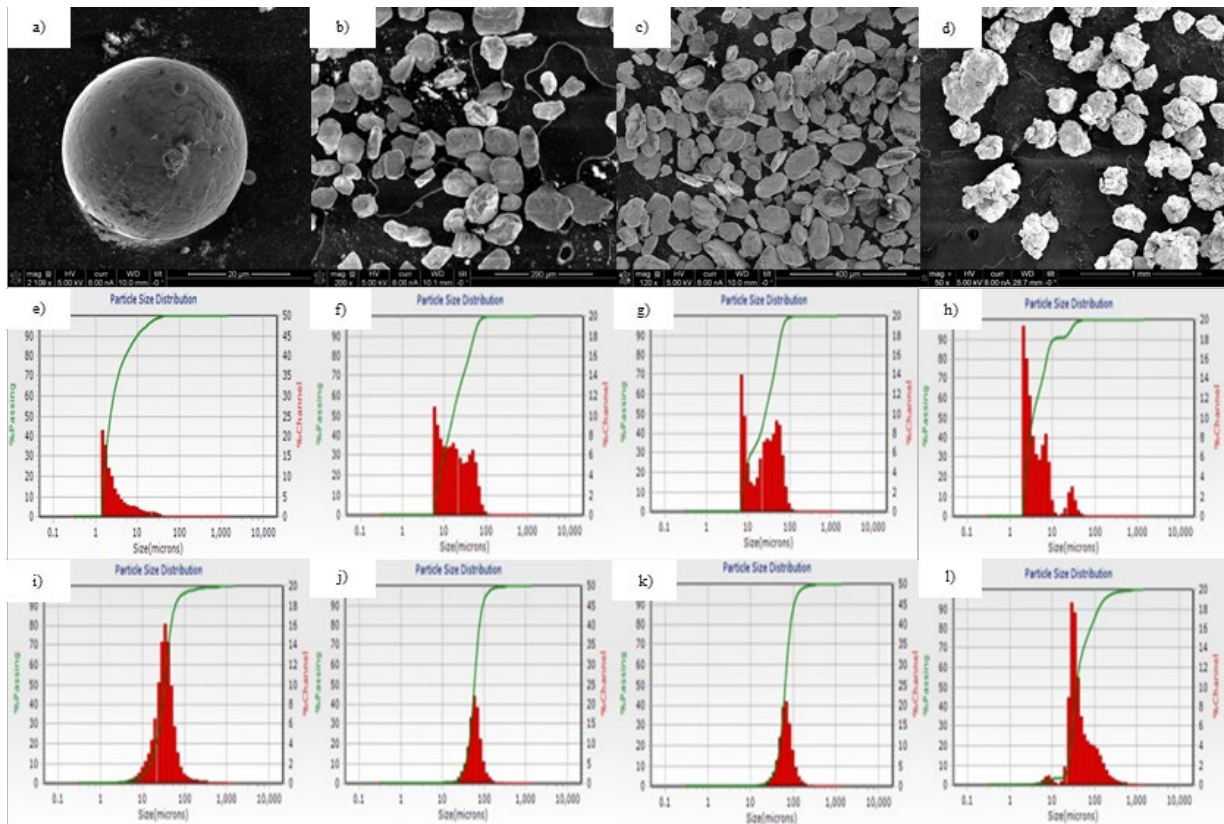


Figure 2.8: Powder size distribution and morphology: Secondary electron picture of a) pure Hastelloy N b) Cryo A c) Cryo B d) ball milled powder. Number size distribution of e) pure Hastelloy N f) Cryo A g) Cryo B h) ball milled powder. Volume size distribution of i) pure Hastelloy N j) Cryo A k) Cryo B l) ball milled powder.

Cryo-milled B batch and ball-milled powder were also analyzed through SEM, as shown in Figure 2.8.b and 2.8.c, respectively. The batch cryo-milled for 8 hours shows a flaky morphology. Meanwhile, the ball-milled samples have an irregular morphology. The flaky morphology is expected after milling, while the irregular morphology indicates over-milling of the powder. Figure 2.8.e and Figure 2.8.f show Cryo B and ball milled powder size distribution and volume distribution, respectively. Table 2.2 summarizes the size density results for Cryo B, which has grown from 1.5  $\mu\text{m}$  before milling to 6.16  $\mu\text{m}$ , indicating coarsening of the powder particles. This is consistent with the volumetric size distribution. This result also applies to the ball-milled sample. However, the density shows that the powder has many fines since D90 is 10.36  $\mu\text{m}$  compared to a D90 of 55.43  $\mu\text{m}$  for the Cryo B sample and a D90 of 9.98  $\mu\text{m}$  for the pure powder. This indicates that the powder was heavily fractured. These powders may lead to the formation of layer defects during LPBF because of the poor spread ability.

Table 2.2: Laser granulometry measurement of the different powders

Powder	Number density distribution			Volumetric density distribution		
	D <sub>10</sub> ( $\mu\text{m}$ )	D <sub>50</sub> ( $\mu\text{m}$ )	D <sub>90</sub> ( $\mu\text{m}$ )	Dvol <sub>10</sub> ( $\mu\text{m}$ )	Dvol <sub>50</sub> ( $\mu\text{m}$ )	Dvol <sub>90</sub> ( $\mu\text{m}$ )
Hastelloy N	1.51	2.26	9.98	15.55	32.75	59.46
<i>Cryo A</i>	6.47	16.34	51.71	36.28	58.3	90.61
Cryo B	6.16	19.58	55.43	40.18	64.65	103.70
Ball milled	2.15	3.42	10.36	24.40	36.65	123.80



The oxides seem more prominent in the powder than in the consolidated samples, as seen in Figure 2.10. This indicates that the addition of Ti and Zr didn't form an oxide a Y-Zr-O-type or a Y-Ti-O at this point. This also has been observed in the literature[38]. Zr has dissolved at elevated temperatures with  $Y_2O_3$  to form Y-Zr-O, which is smaller in size. TEM images shows that there is some Zr, which is not in the form of an oxide. After the annealing of the samples, Y-Zr-O formed. This can be seen in the diffraction pattern of the samples. The incorporation of Zr led to the refinement of these oxides. This is also shown in the Cryo B powder that Ti didn't dissolve fully.

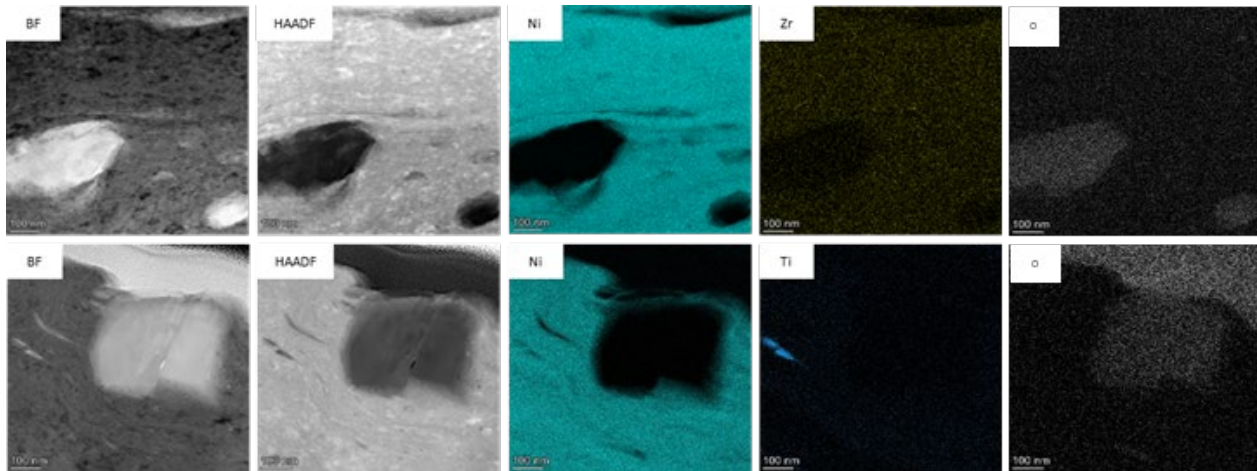


Figure 2.10: Top: STEM-EDS maps of the Cryo A samples, bottom: STEM-EDS maps of the Cryo B samples.

#### IV. Consolidation of the powders through cold pressing followed by sintering

The process here consists of cold pressing different powders and then sintering at high temperature for a given amount of time. The different parameters are shown in Table 2.3

Table 2.3: shows the conditions used in the process.

Sample	Powder	Pressure (psi)	Temperature (C°)	Time (hours)
M1	Pure Hastelloy N	2200	1125	2
M2	UCB milled	2200	1125	2
M3	Cryo milled (batch A)	1500	1125	2
M4	Cryo-milled (batch A)	2100	1200	2
M5	Cryo-milled (batch A)	2200	1125	6
M6	Cryo-milled (batch B)	2200	1125	2

#### V. Additive manufacturing

The additive manufacturing machine used to print the samples from the powders was a laser powder bed fusion machine available at the CAMAL facility at NCSU. It uses a modified concept laser M100R with a 100-W Nd:YAG fiber laser at 1060 nm wavelength and 50 lm spot size. Prior to consolidation the samples were designed using CAD software.

During the printing process, the laser scans the powder, thus, melting the powder and solidifying into the alloy. Once the first layer is printed, another layer of powder is disposed over the previous layer.

In addition to the ball milled powder (from NCSU) and the cryo B powder (from UC-Berkeley), pure Hastelloy N powders were also printed as well as a hand blended mixture (mixed by hand shaking) made of Hastelloy N powder with an addition of 1 wt%Ti and 0.5 wt%Y<sub>2</sub>O<sub>3</sub>.

Table 2.4 summarizes the conditions used to make different builds.

Table 2.4: Additively manufacturing of Hastelloy N samples with different parameters and composition

Sample name	Powder type	LPBF parameters					
		Sample Diameter (mm)	Height (mm)	Beam speed (mm/s)	Hatch Spacing (mm)	Layer Thickness (mm)	Laser power (J)
		<i>P1</i>	Hastelloy	6.3	6.5	1000	0.05
<i>P2</i>	6.25	1000					
<i>P3</i>	6.3	760					
<i>P4</i>	Ball milled	6.3	2.9	1000			
<i>P5</i>		6.25		1000			
<i>P6</i>		6.3		760			
<i>P7</i>	Cryo B	6.3	5	1000			
<i>P8</i>		6.3		608			
<i>P9</i>		6.25		760			
<i>P10</i>	Blended	6.3	3	1000			
<i>P11</i>		6.3		608			
<i>P12</i>		6.25		760			

## VI. Pycnometer density measurements

The samples in Table 2.4 fabricated via additive manufacturing were cleaned in an ultrasonic bath of ethanol for 5 minutes; then dried and their weight was measured. Density measurements were carried out using a Quantachrome Ultrapyc 1200e. An inert gas penetrates the porosities without interacting with the surface chemistry. This ensures the highest quality result. Helium is generally used in these types of experiments. However, in our case, nitrogen was used which does not provides the same degree of precision. Figure 2.11 shows the machine.



Figure 2.11: Picture of the Quantachrome Ultrapyc 1200e.

A cell chamber of known volume is put under specific pressure chosen pre-test. Once stable, the machine will record the pressure. A valve is then opened, allowing the expansion of the gas into the reference chamber, which also has a known volume. Once stable, this second pressure will also be recorded. The drop ratio is measured and compared to the system behavior when a known volume undergoes the same process. Accurate results on a gas pycnometer are ensured by a proper ratio between the reference volume and the sample chamber's volume. Suppose this value is too small or too large. The subsequent pressure drops created during the analysis will lead to inaccuracies.

## Chapter 3: Results

### I. Hastelloy N Sintered samples

#### I.1 General description of the microstructure of the sintered samples

Table 3.1 presents the different sintered samples list and the processing conditions

Table 3.1: Parameters used to consolidate the sintered samples.

Sample	Powder	Pressure (psi)	Temperature (C°)	Time (hours)
M2	UCB mechanically alloyed sample	2200	1125	2
M3	Cryo milled (batch A)	1500	1125	2
M4	Cryo-milled (batch A)	2100	1200	2
M5	Cryo-milled (batch A)	2200	1125	6
M6	Cryo-milled (batch B)	2200	1125	2

#### I.1.1 UCB mechanically alloyed powder cold-pressed at 2200 psi sintered at 1125°C for 2h M2 sample characterization

This sample was made from powder mechanically alloyed in house at UCB using their attritor (not cryo-milled). Transmission electron microscopy of M2 sample is shown in Figure 3.1. The microstructure is composed of nanostructured grains that are irregular and elliptical. No evidence of carbide at this state of the process.

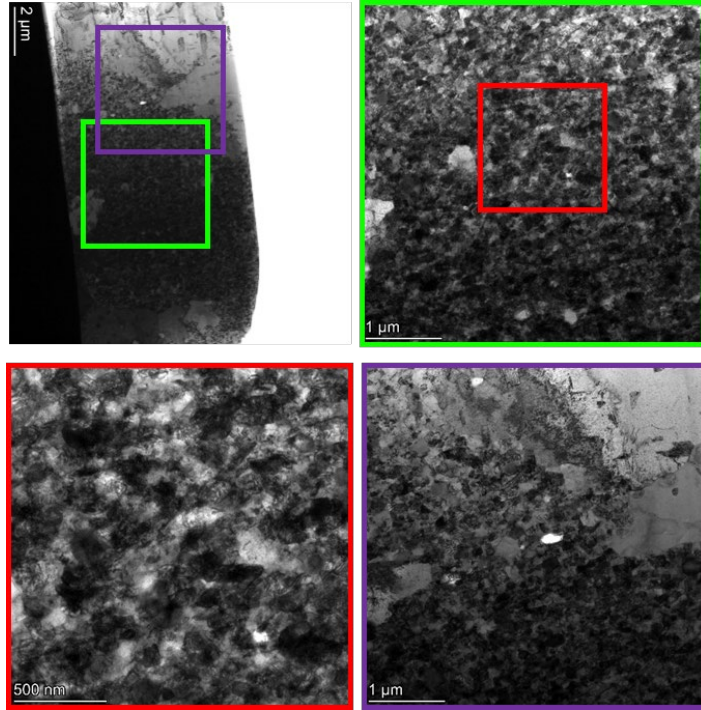


Figure 3.1: TEM image of the Sample M2

STEM-EDS map detailing the microstructure and the chemical composition of different features is shown in Figure 3.2. This figure shows alongside oxide particles the existence of (Mo, Si) enriched grains.

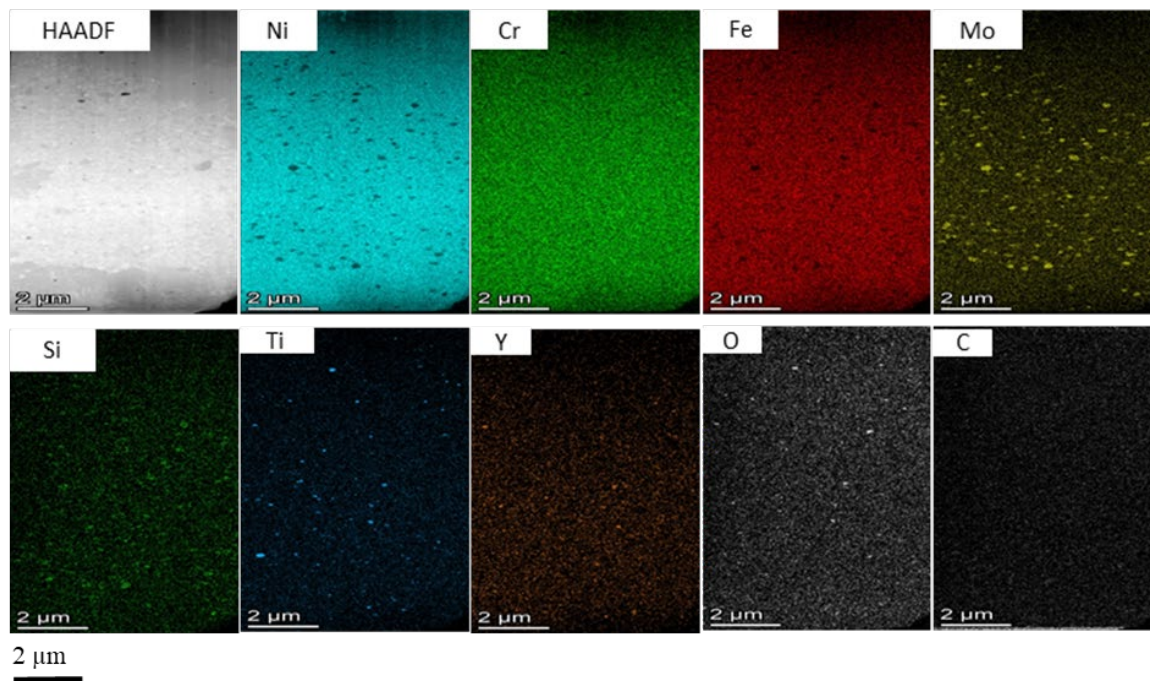


Figure 3.2: STEM-EDS maps of the house sample M2

### I.1.2 Cryo A 1500 psi 1125°C for 2h sample (M3)

Figures 3.3 and 3.4 show TEM and the STEM-EDS chemical maps of Cryo-milled A powder cold pressed at 1500 psi and sintered at 1125°C for 2h.

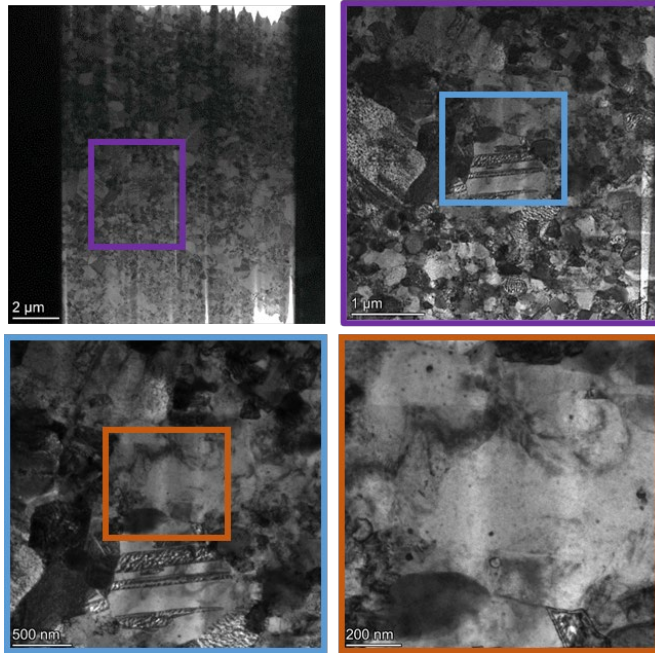


Figure 3.3: TEM of M3 sample.

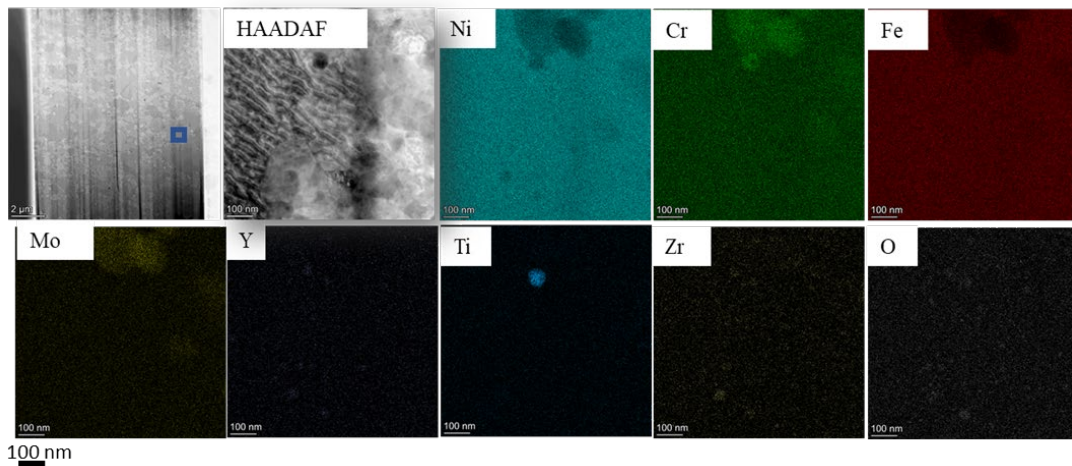


Figure 3.4: STEM-EDS chemical maps of M3 sample.

### I.1.3 Cryo A 2100 psi 1200C for 2h sample (M4)

Figure 3.5 shows of the M4 sample, and Figure 3.6 shows the STEM-EDS.

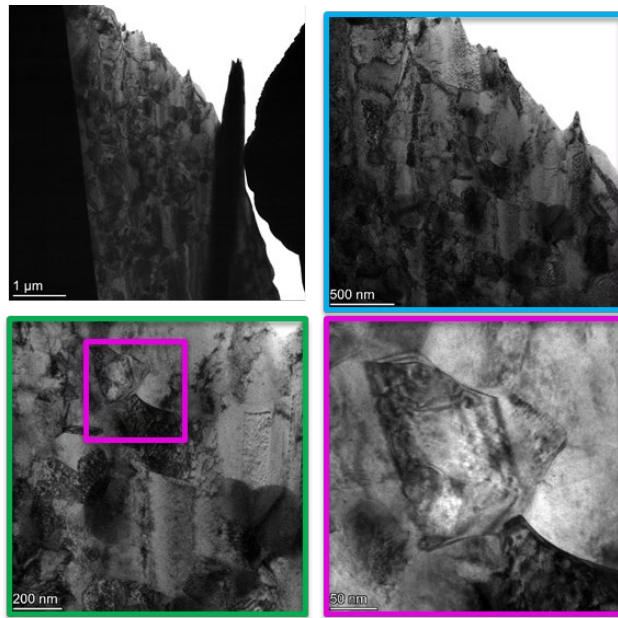


Figure 3.5: TEM pictures of M4 sample

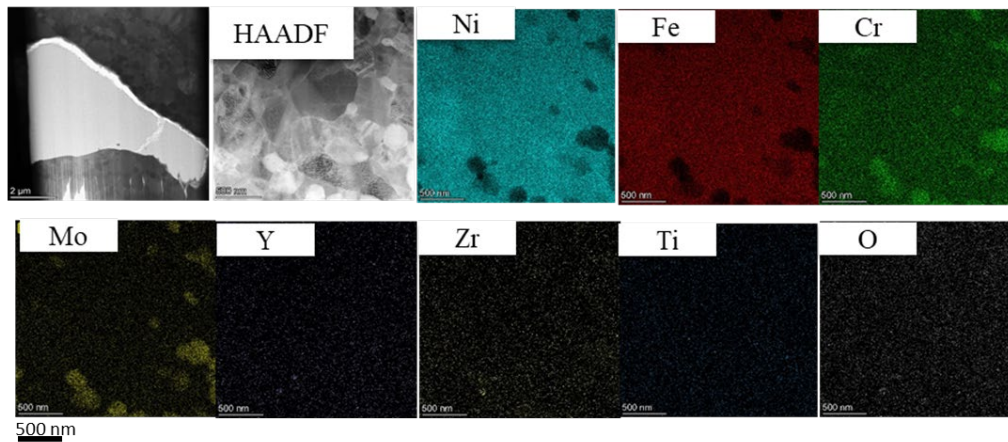


Figure 3.6: STEM-EDS chemical maps of M4 sample

### I.1.4 Cryo A 2200 psi 1125C for 6h sample (M5)

Figures 3.7 and 3.8 show the TEM and STEM-EDS chemical maps of the Cryo A 2200 psi 1125C for 6h sample.

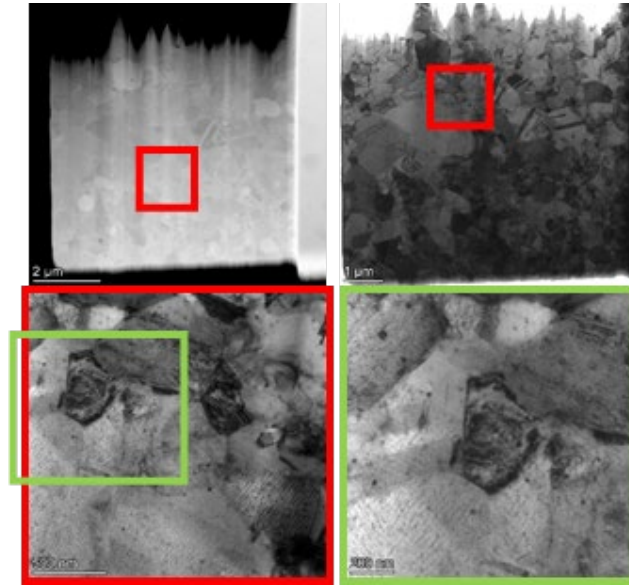


Figure 3.7: TEM of sample M5.

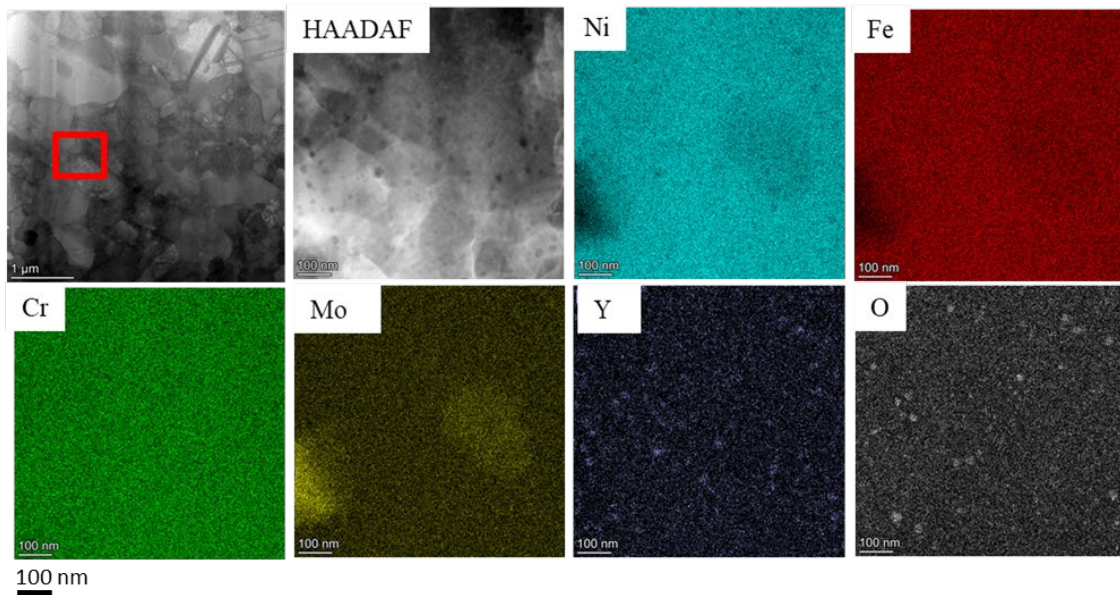


Figure 3.8: STEM-EDS chemical maps of M5 sample

### I.1.5 Cryo B sample M6 description

Figure 3.9 shows Cryo B TEM images. Showing slightly bigger grains than the house sample. Some grains that are enriched in Mo, Si, and Cr, as shown in Figure 3.10.

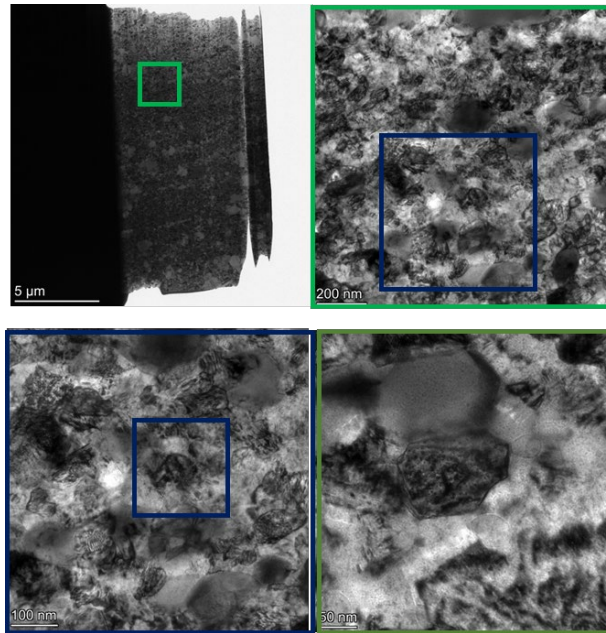


Figure 3.9: TEM of M6 sample.

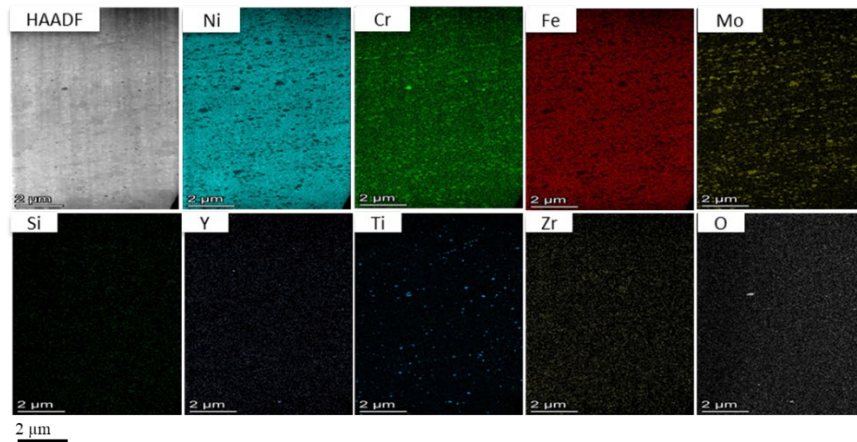


Figure 3.10: STEM-EDS chemical maps of the Cryo B M6.

## I.2 Oxide size measurements

The oxides were measured on the STEM images (with help of the chemical maps to identify the oxides) and the thickness of the TEM samples was averaged over the thickness maps obtained with the Talos TEM microscope at NCSU. The overall results are reported in Table 3.2. The particle size was determined by assuming an elliptical shape for the 2D projection of the precipitates on the STEM images and measuring two diameters for every oxide using image J software, then the area of the ellipse was calculated and an equivalent diameter was derived assuming a disc of equal area.

Table 3.2: Particle size distribution.

Sample	Mag.	Average particle (nm)	D10 (nm)	D90 (nm)	D50 (nm)	Number density (# of particle/m <sup>3</sup> )	Volume fraction	Thickness (nm)	Particle count
M2	125Kx	46.355	22.89	33.59	85.79	$8.76 \times 10^{19}$	1.184	126.43	10
	45 Kx	73.10	27.55	50.08	150.1	$1.737 \times 10^{19}$	1.0624	116.13	10
M3	125 Kx	22.05	12.34	28.00	18.368	$3.38 \times 10^{20}$	0.618	197.90	42
	125 Kx	42.017	16.30	72.49	29.28	$9.11 \times 10^{19}$	0.9349	191.72	10
M4	32Kx	18.506	8.83	20.78	14.01	$2.59 \times 10^{20}$	0.211	123.93	157
M5	125 Kx	21.68	13.16	30.20	20.37	$9.40 \times 10^{20}$	0.8622	192.54	114
	125 Kx	21.49	13.36	32.39	19.52	$7.898 \times 10^{20}$	0.582	210.12	103
M6	45 Kx	46.92	31.21	88.91	43.67	$1.104 \times 10^{20}$	1.255	93.74	52
	125 Kx	39.53	15.43	79.06	24.64	$1.107 \times 10^{20}$	1.032	143.35	10

### **I.2.1 Oxide particle characterization of M2 House sample**

Figures 3.11 through 3.15 show the images used to measure the oxides for each sample (M2, M3, M4, M5, M6)

The M2 sample, ball milled, has an average oxide size of 56.8 nm, calculated from two TEM images through 20 particles. The number density is  $2.44 \times 10^{19}$  particles /m<sup>3</sup> and a volume fraction of 1.09%. Figure 3.11 shows the TEM image of a region where the oxide measurement was conducted.

The M3 sample seems to have a small average oxide particle size of 26.19 nm measured through two TEM images with a total particle count of 52, an average density of  $4.38 \times 10^{20}$  particle/ m<sup>3</sup>, and a volume fraction of 0.77%. The STEM-EDS maps of the M3 sample are shown in Figure 3.12.

M4 sample oxide measurement was conducted using ImageJ. The time and temperature seems to play a significant role in oxide size distribution this will be discussed with more details in chapter 4. The smallest size of oxides was obtained in with higher temperatures annealing. However, the volume density was the lowest in the case of M4, suggesting that a higher temperature might not be very efficient in terms of desired microstructure in terms of oxide volume and distribution. Figure 3.13 shows the STEM chemical map of the M4 sample.

From Table 3.2, the M5 sample has the smallest average oxide particle size of 21.60 nm for both TEM images analyzed with 217 particle count, and a number density of  $9.01 \times 10^{20}$  particle/m<sup>3</sup> and a volume fraction of 0.75%. The volume fraction is not the highest of the samples, but other samples, like the UC Berkeley sample M2, are agglomerated and have higher oxide particle additions. Figure 3.14 shows the chemical maps used to measure the oxide thickness, and

from these maps, the complex composition of some oxides is revealed, which seem to be enriched in Zr and Y, especially the bigger oxides.

M6 sample is also cryo-milled; however, it shows a bigger average particles size of 48.39 nm with a sample density number of an average of  $9.26 \times 10^{19}$  particles/  $m^3$  and a volume fraction of an average of 1.05 %. Figure 3.15 shows a chemical map of a region where the measurement was taken. Here it is observed that some grains are enriched in Cr, Ti, and Mo.

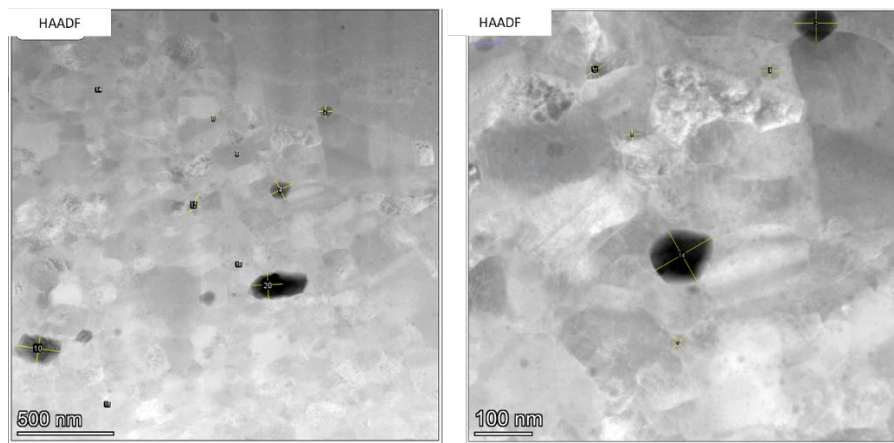


Figure 3.11: Oxide measurements for M2 sample

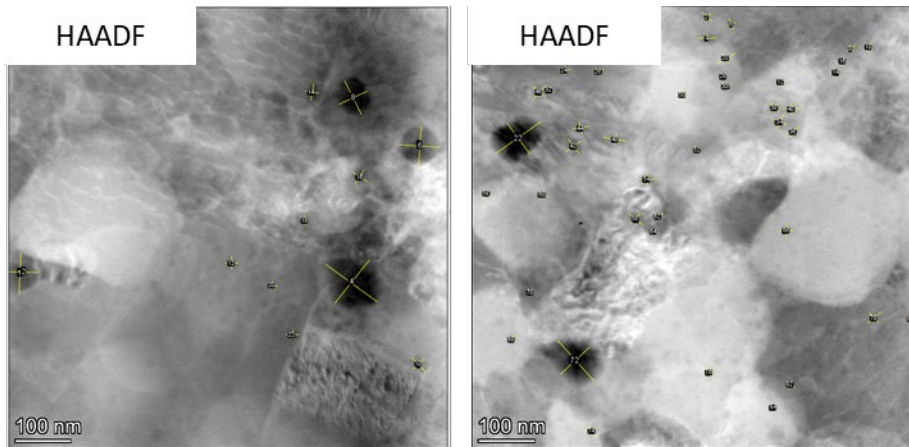


Figure 3.12: Oxide measurements for M3, Cryo A 1500 psi 1125°C for 2h

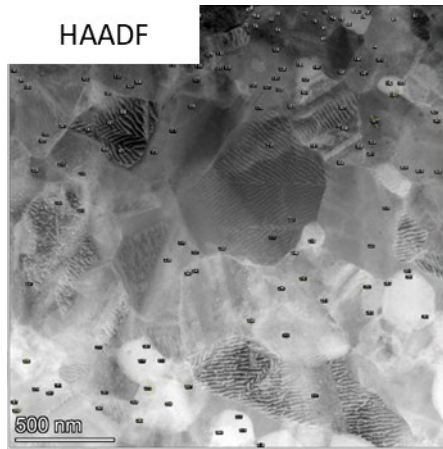


Figure 3.13: Oxide measurements for M4 Cryo A 2100 psi 1200°C for 2h.

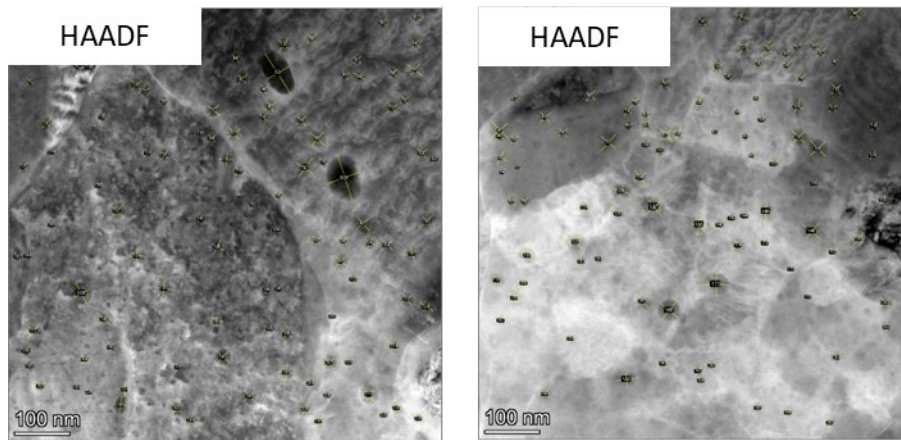


Figure 3.14: Oxide measurements for the M5, Cryo A 2200 psi 1125°C for 6h

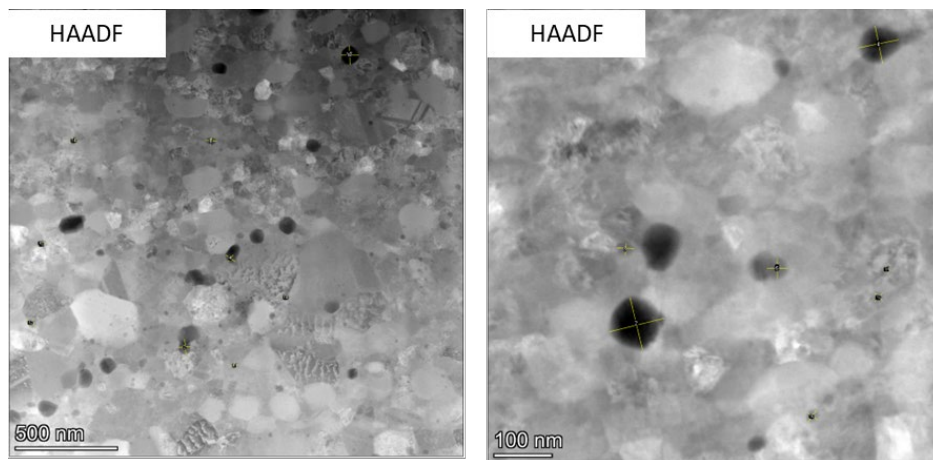


Figure 3.15: Oxide measurements for the M6 sample Cryo B 2200 psi 1150°C for 2 hours

## II. Hastelloy N additive manufactured samples

Twelve Hastelloy N Samples were made through LPBF AM at the Center for Additive Manufacturing and Logistics (CAMAL) located at North Carolina State University. The samples were cylindrical, with diameters about 6.3 mm. The samples were fabricated upon steel substrates. Figure 3.16 shows the different samples made.



Figure 3.16: Photograph showing the Hastelloy N samples fabricated by LPBF

As a reminder, Table 2.4 shows the details of the LPBF parameters used for the AM printing of the samples as well as which powder was used in each case.

### II.1 Density measurements

P1, P2, and P3 were made up of Hastelloy N powder. P7, P8, and P9 were made up of cryo-milled B powder, and P10, P11, and P12 were fabricated using 98.5% Hastelloy N powder, 0.5%  $Y_2O_3$ , and 1% Ti (hand shaken), (P4, P5, P6 samples were too small to be measured for density through the technique used hereby). Note that Hastelloy N density is 8.89 g/cc, and none of the measurements exceeded this value which is a good sign. The machine margin of error doesn't seem to be small since the chamber [26] is much larger than the actual sample.

Table 3.3: LPBF parameters used for the AM printing of the samples

Sample	Powder	Sample weight (g)	average volume (trial 1) (cc)	average volume (trial 2) (cc)	average volume (trial 3) (cc)	Average standard deviation	Average Density (g/cc)
P1	Hastelloy N	1.39	0.158	0.156	0.157	0.0001	8.82
P2	Hastelloy N	1.4008	0.160	0.160	0.160	0.00006	8.76
P3	Hastelloy N	1.362	0.154	0.154	0.155	0.00013	8.82
P7	Cryo B	1.010	0.125	0.126	0.126	0.00013	8.06
P8	Cryo B	0.939	0.113	0.113	0.113	0.00013	8.33
P9	Cryo B	0.930	0.114	0.115	0.115	0.00006	8.11
P10	Blended	0.707	0.080	0.080	0.080	0.00016	8.83
P11	Blended	0.559	0.064	0.064	0.064	0.0002	8.71
P12	Blended	0.640	0.074	0.074	0.074	0.00013	8.67

### II.1.1 Microstructural characterization of the LPBF samples

#### a) TEM characterization of sample P3

TEM images of the P3 sample are shown in Figure 3.17. The P3 sample consists of pure Hastelloy N powder.

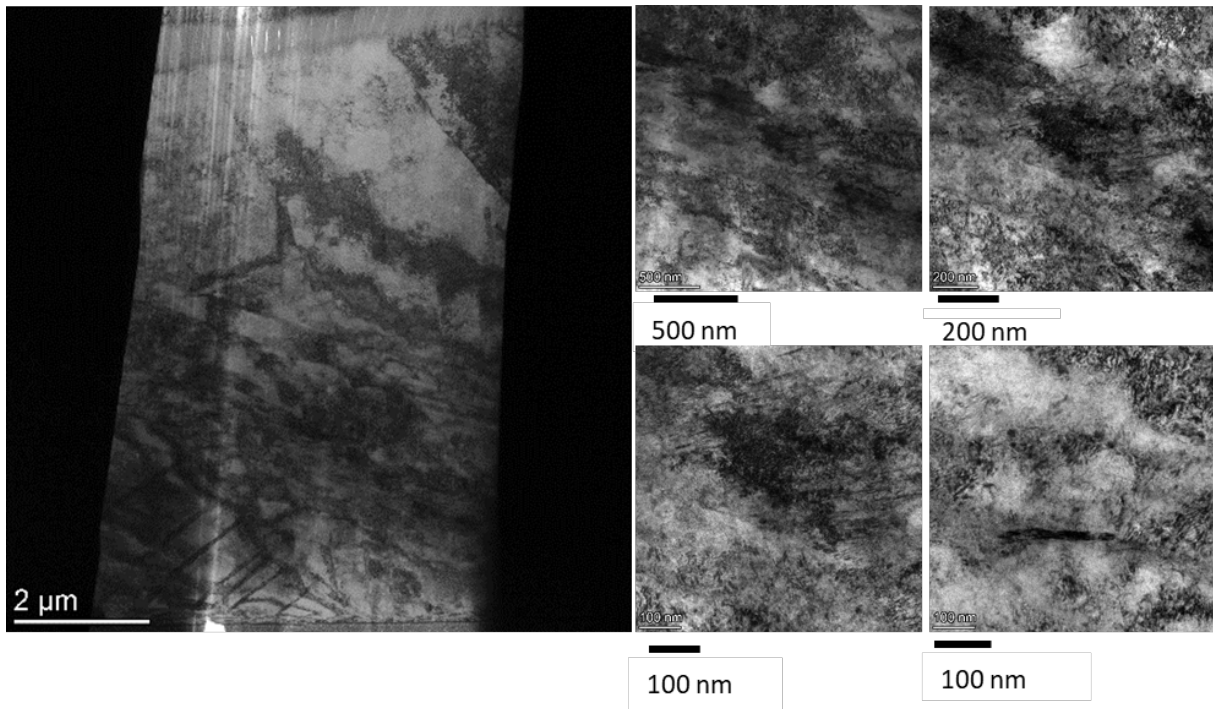


Figure 3.17: TEM images of Hastelloy N P3 Sample

Figure 3.18 shows the STEM-EDS chemical maps of P3.

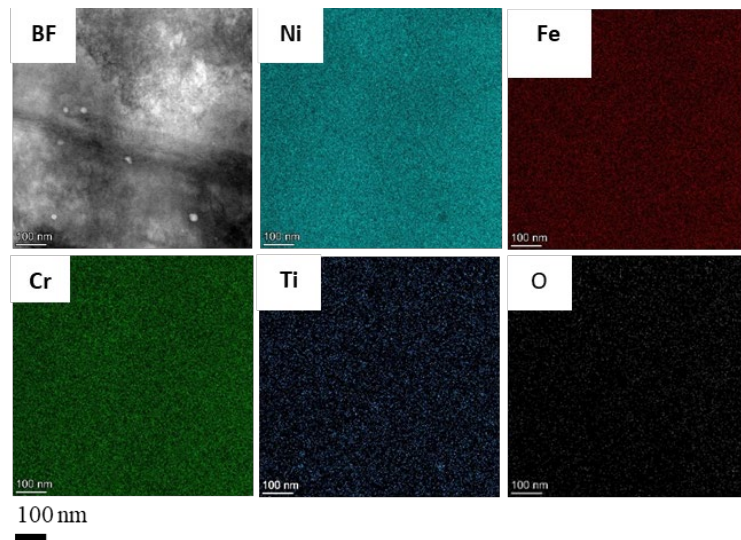


Figure 3.18: STEM-EDS maps of P3 sample showing Ni, Cr, Fe, Ti, O, Y.

### b) TEM characterization of samples P6 and P4

Figure 3.19 and Figure 3.20 show the TEM images and chemi-STEM maps for sample P6 respectively.

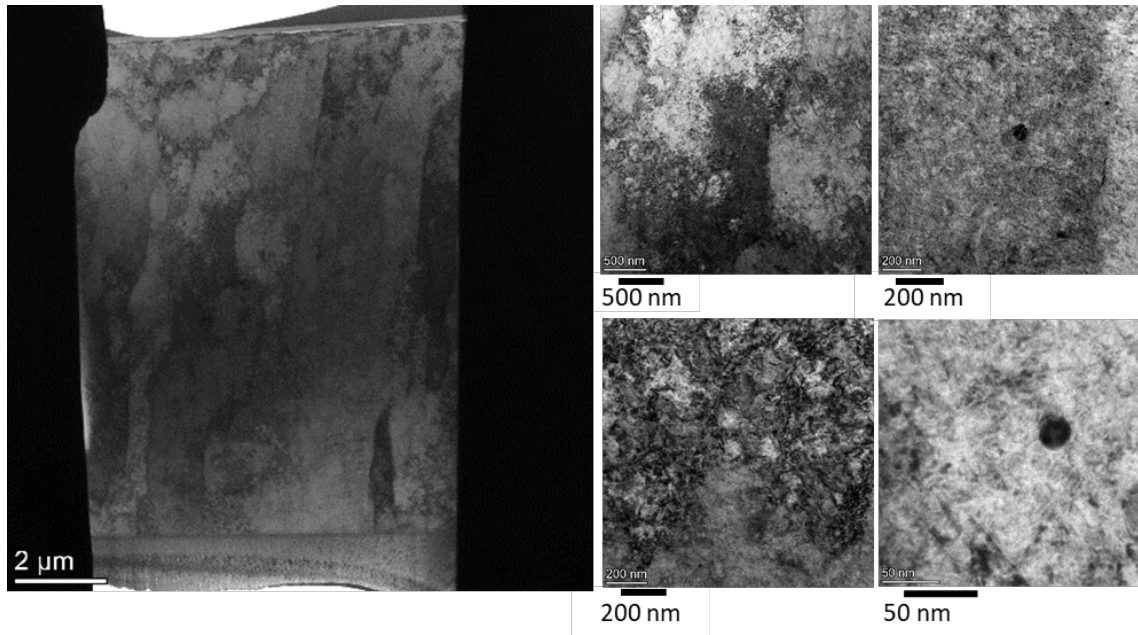


Figure 3.19: TEM images of sample P6 sample

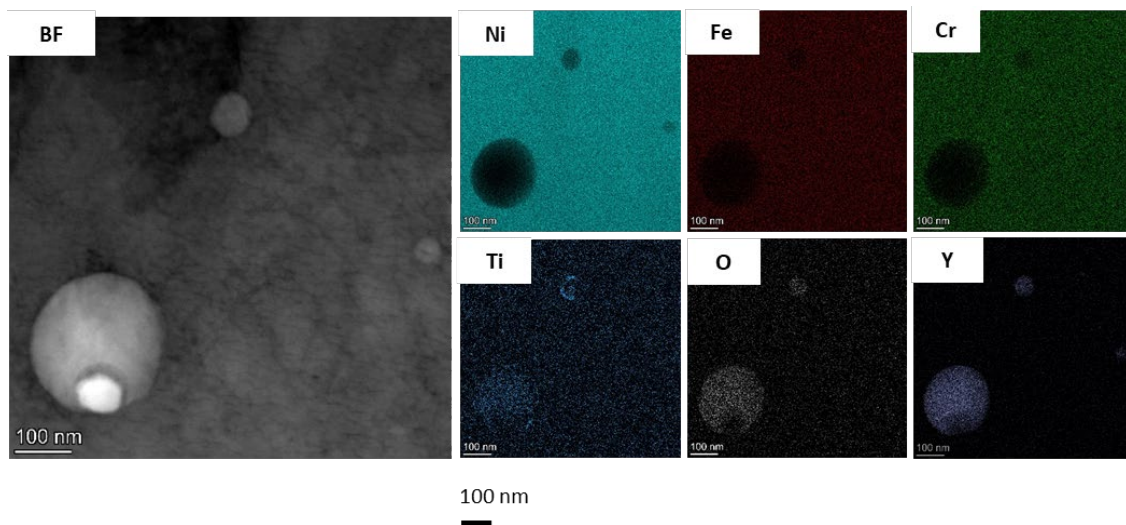


Figure 3.20: STEM-EDS maps of sample P6.

For comparison, P4 was also analyzed, as shown in Figure 3.21 and STEM-EDS in Figure 3.22

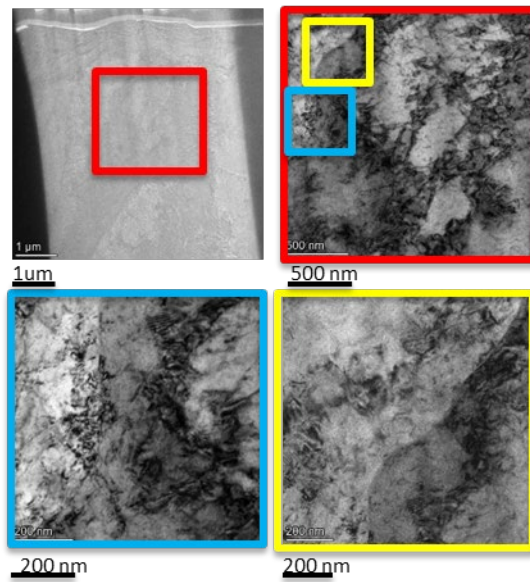


Figure 3.21: TEM pictures of sample P4.

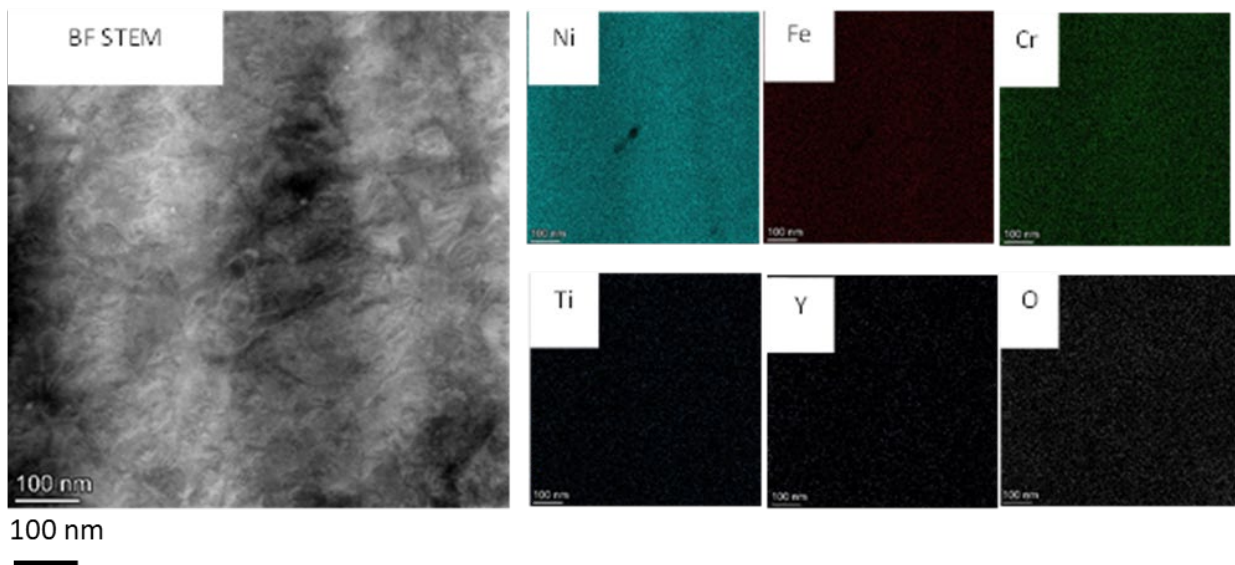


Figure 3.22: STEM-EDS pictures of sample P4.

### c) TEM characterization of samples P9 and P7

Figure 3.23 show the TEM images of P9. The high mags pictures show a spherical defect that might be a cavity. These multiple small cavities could explain the lower density of the cryo-milled powder.

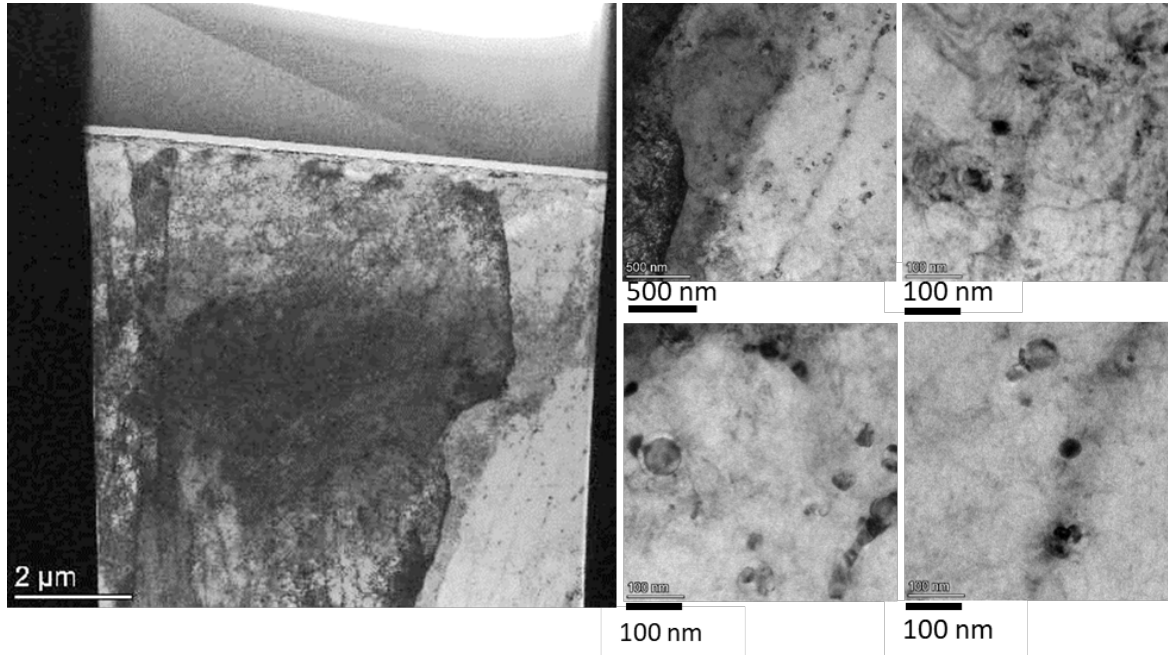


Figure 3.23: TEM picture of sample P9

Figure 3.24 shows the STEM-EDS images of the P9 sample, which is a Cryo B sample. As shown P9 has more oxide particles that are uniformly distributed.

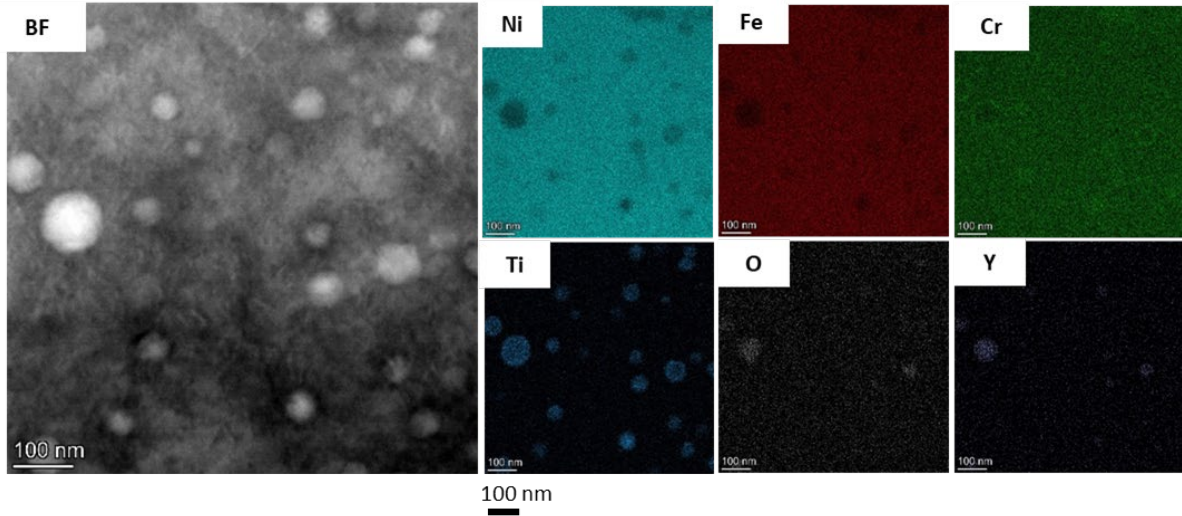


Figure 3.24: STEM-EDS maps of sample P9

TEM and STEM-EDS maps show a similar oxide density for the P7 sample in Figure 3.25 and Figure 3.26

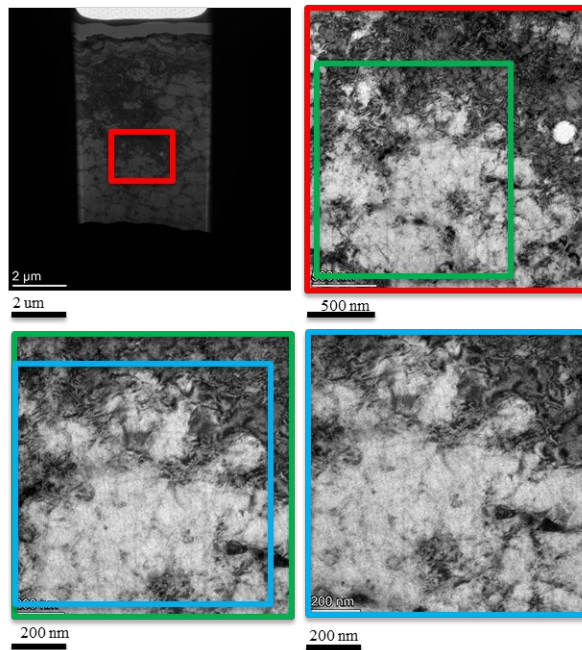


Figure 3.25: TEM picture of P7

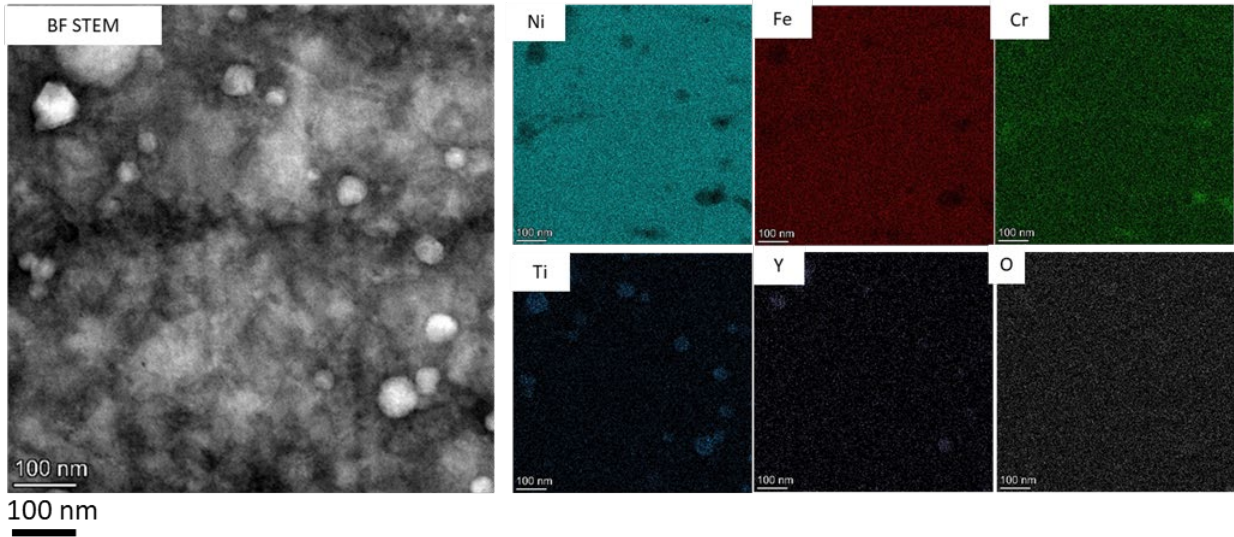


Figure 3.26: STEM-EDS maps of P7

**d) TEM characterization of sample P12 and P10**

Figure 3.27 shows TEM images of P12; it clearly shows the work hardened surface region due to poor sample preparation.

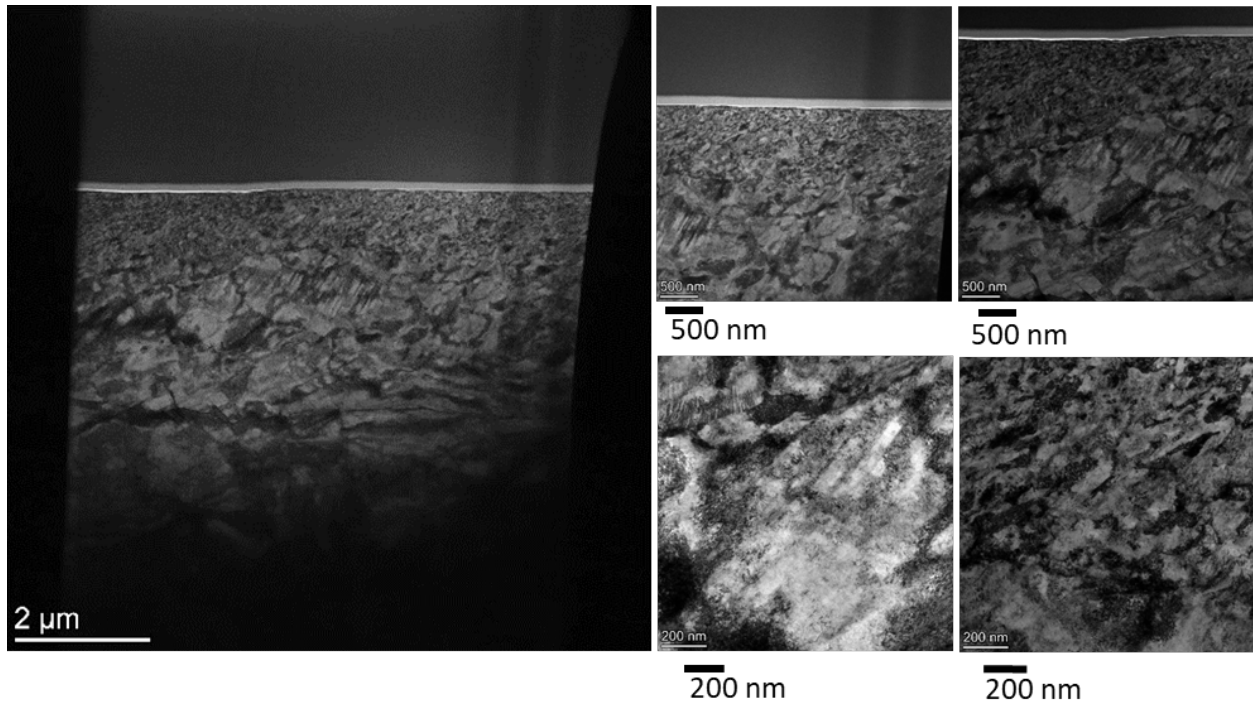


Figure 3.27: TEM images of sample P12

Figure 3.28 shows the STEM-EDS chemical of P12.

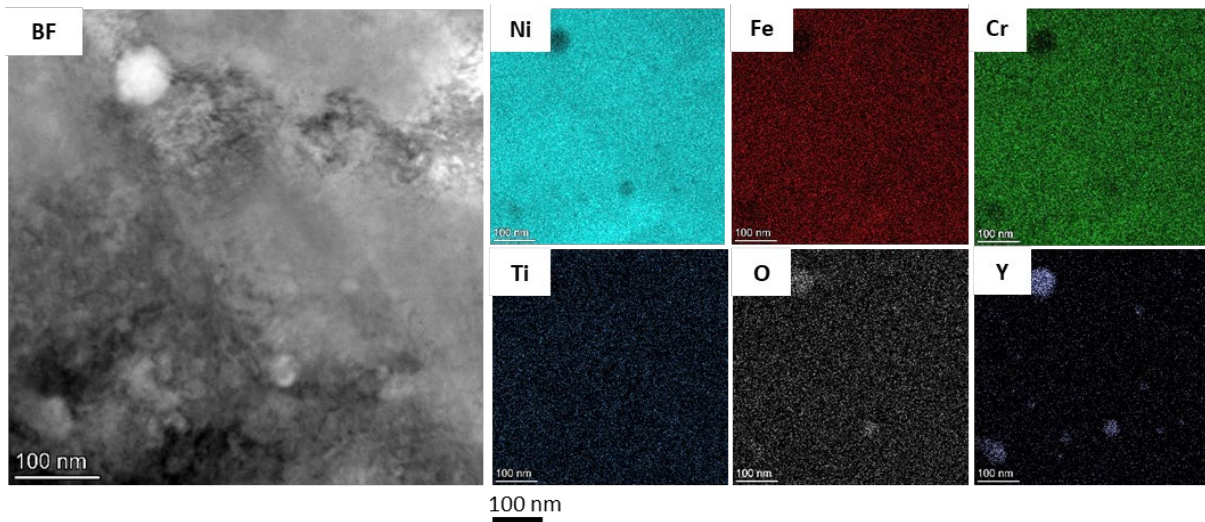


Figure 3.28: STEM-EDS images of sample P12.

For comparison, the P10 sample was analyzed. TEM images and STEM-EDS are shown in Figure 3.29 and 3.30.

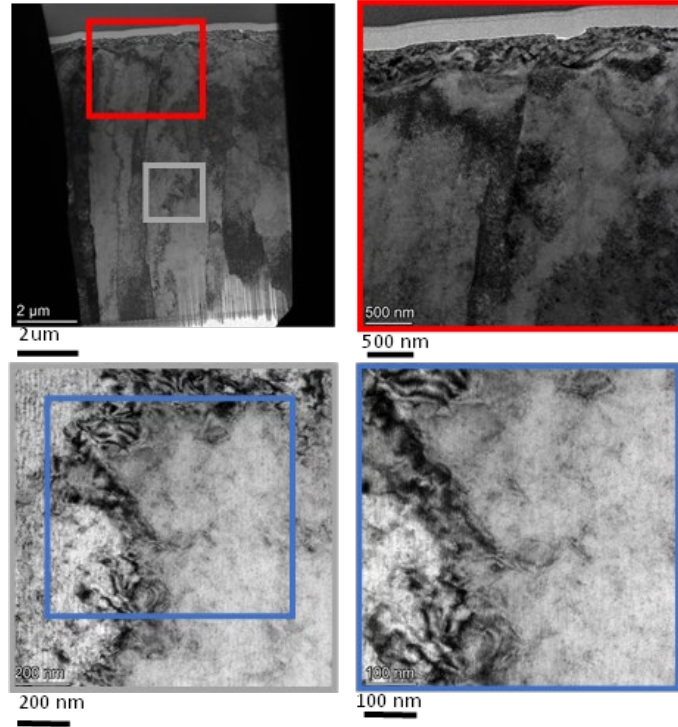


Figure 3.29: TEM pictures of P10 samples.

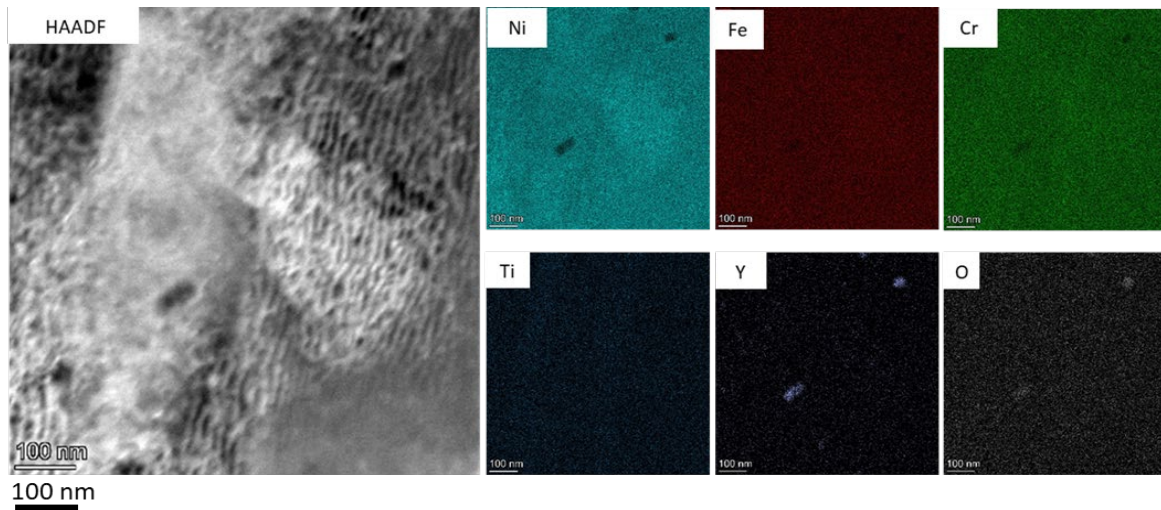


Figure 3.30: STEM-EDS pictures of P10 samples

## II.2 Oxide size measurement

Table 3.4 summarizes the oxide measurements for the additive manufactured P-samples

Table 3.4: Oxide size measurement for the additive manufactured P-samples

Sample	Mag (Kx)	Average adequate size (nm)	D10	D90	D50	Number density (particles/m <sup>3</sup> )	Volume percent	Thickness	Particle count
P6	125	45.27	18.77	60.39	44.53	$9.384 \times 10^{19}$	0.49	188.70	11
	45	41.04	24.08	43.62	79.67	$2.11223 \times 10^{19}$	0.189	179.31	19
P9	125	53.53	38.96	68.99	50.01	$1.6318 \times 10^{20}$	1.77	215.67	24
	45	47.88	28.98	64.70	44.88	$1.27865 \times 10^{20}$	1.13	160.94	101
P12	125	19.36	9.74	28.94	16.80	$1.689 \times 10^{20}$	0.137	122.48	13
	125	20.02	10.07	31.01	18.99	$1.2616 \times 10^{20}$	0.085	125.48	10

### II.2.1 Oxide size measurements

Figure 3.31 through 3.33 show the HAADF pictures used to measure the oxide size and number density for samples P6, P9, and P12.

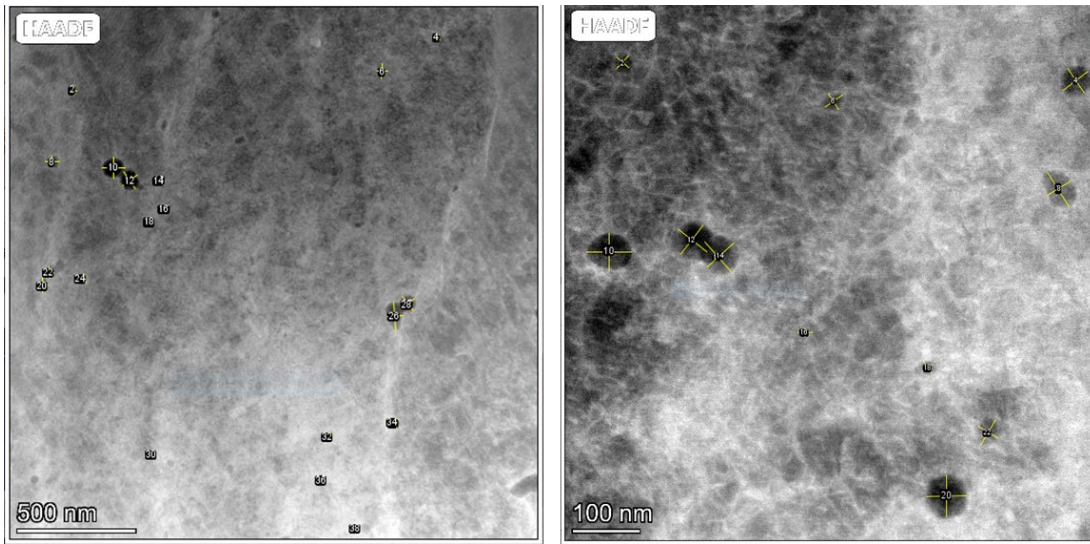


Figure 3.31: Oxide measurements for the P6 sample

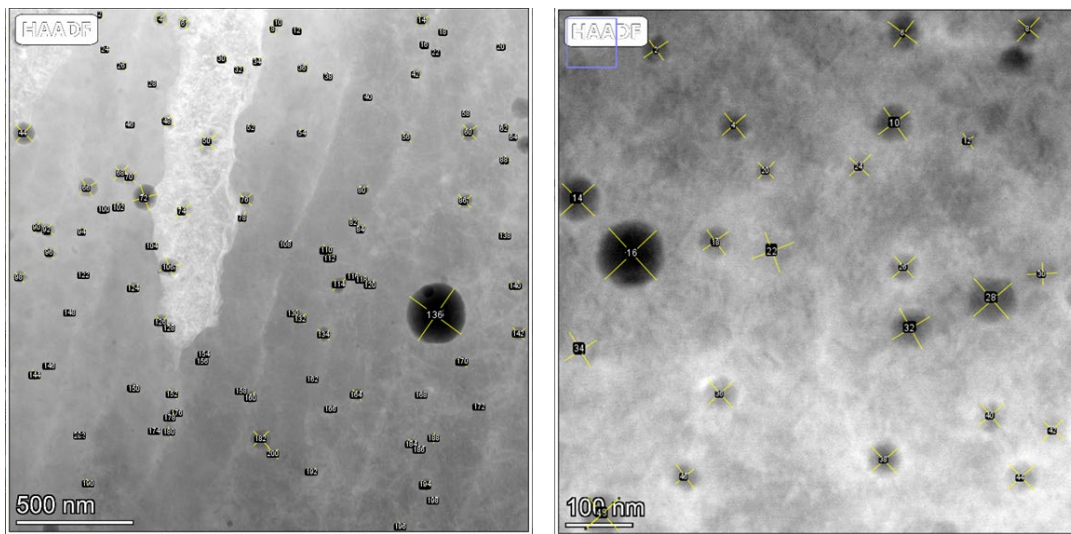


Figure 3.32: Oxide measurements for the P9 sample

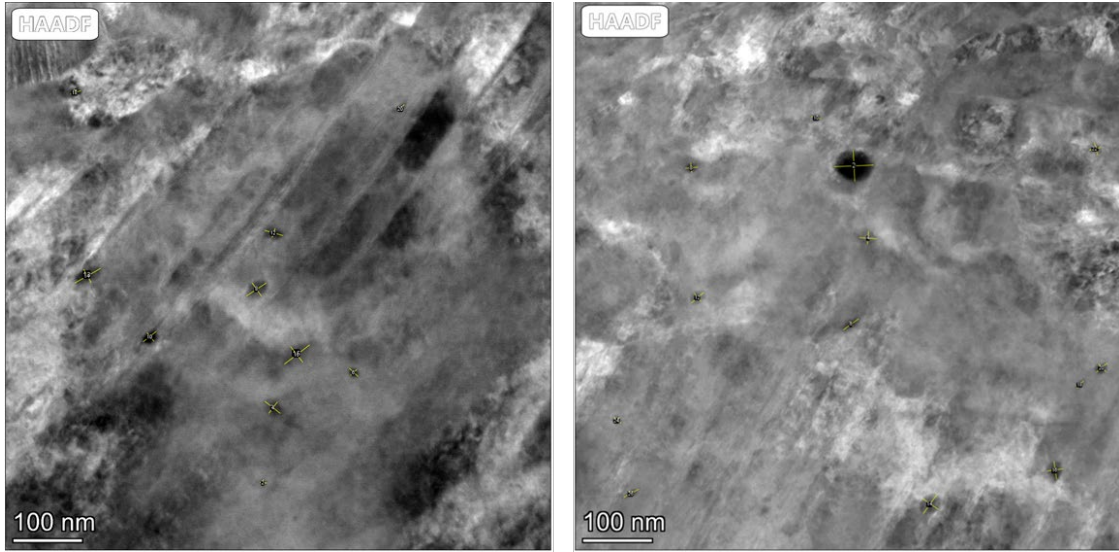


Figure 3.33: Oxide measurements for the P12 sample

## II.2.2 Oxide particle characterization

Figure 3.34 shows the STEM-EDX maps for sample P6. Some particles contain Ti but do not contain Y or O. The oxide particles are more enriched in Y.

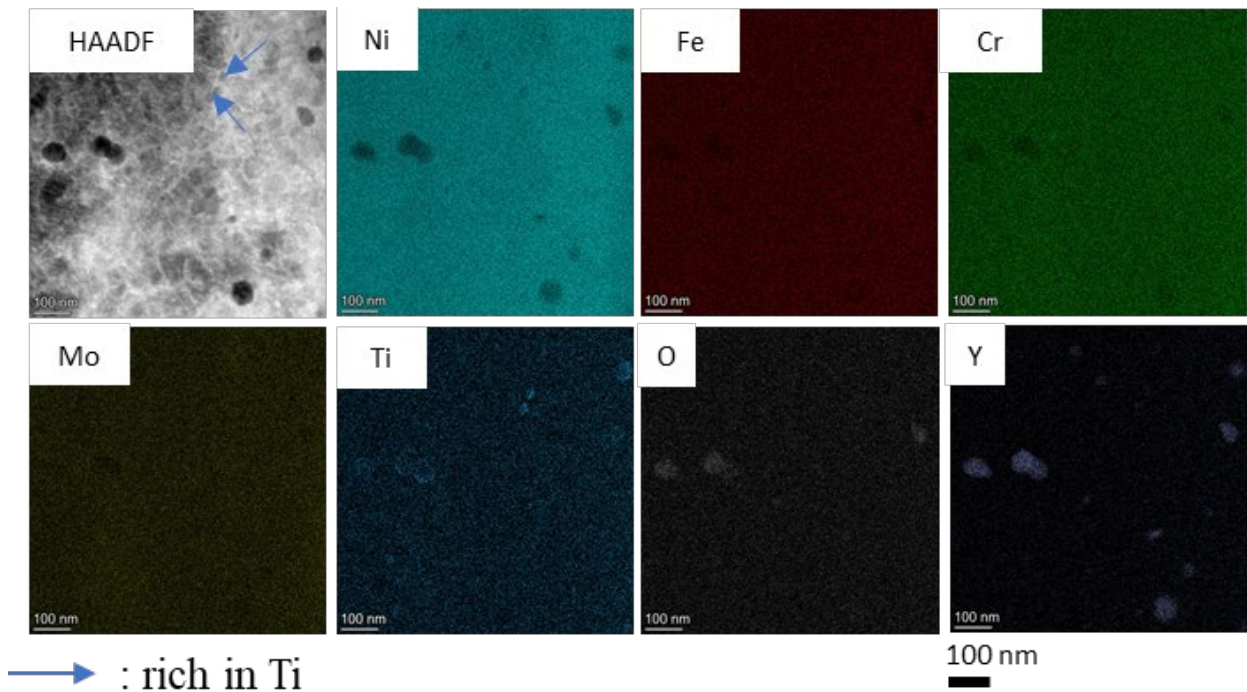
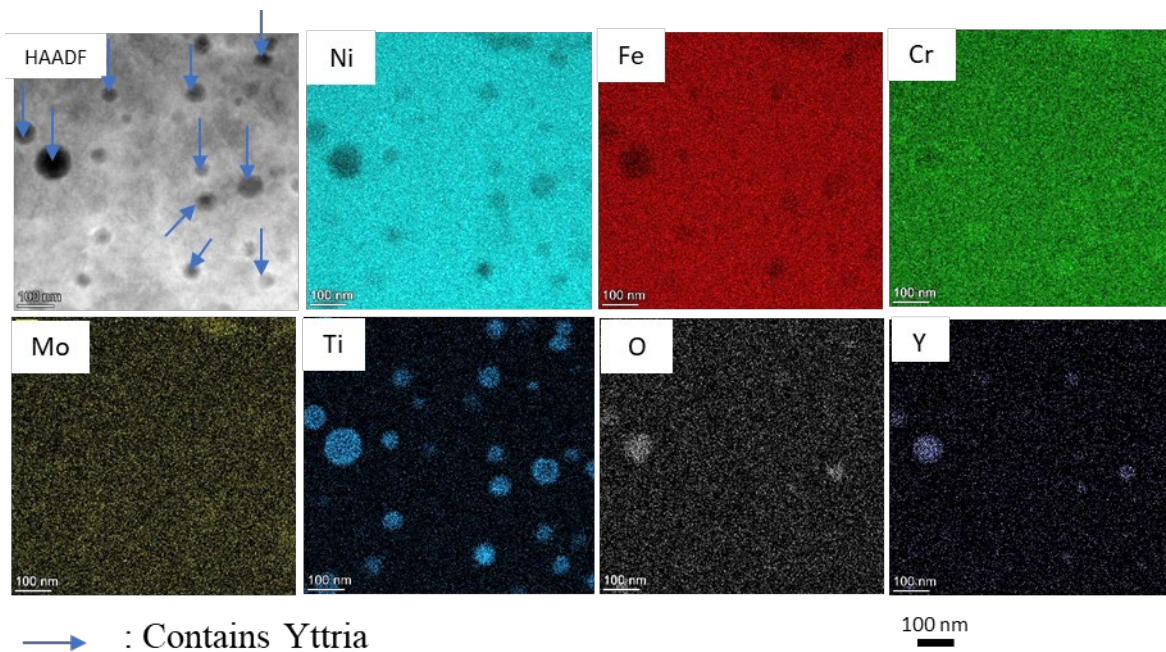


Figure 3.34: STEM-EDS image of the P6 sample.

Figure 3.35 shows the STEM-EDS chemical maps for sample P9 highlighting the particles which contain yttrium. The particles seem to have a variable composition. Some particles are rich in Cr. The coarse particles appear to have an outer ring rich in Cr and an interior depleted in Cr. This core/shell structure of oxide was previously mentioned in the literature [29]. The P9 sample is composed of cryo B powder which includes 0.5% Ti. Most smaller particles are enriched only in Ti, while the coarse ones are rich in oxygen, yttrium, and sometimes Chromium.



**Figure 3.35:** STEM-EDS maps of P9 highlighting the oxide composition

Figure 3.36 shows STEM-EDS maps of P12 Sample. The oxides contain Y, and the bigger ones are depleted in Cr.

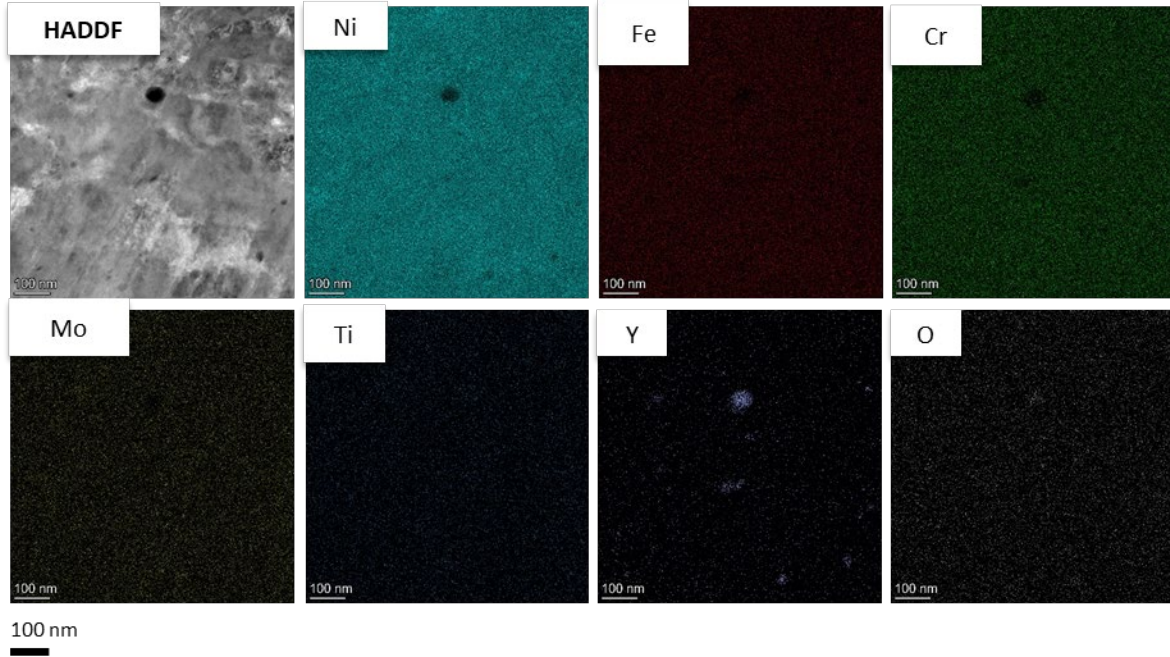


Figure 3.36: STEM-EDS map of P12 Sample.

### II.3 Mechanical properties of the sintered samples

The University of California, Berkeley also conducted nanoindentation hardness testing, and the summary of the results is shown in Table 3.5.

Table 3.5: Hardness of the sintered samples.

Sample	Hardness [GPa]	Std. Dev. [ $\pm$ GPa]	Reduced Modulus [GPa]	Std. Dev. [ $\pm$ GPa]
M1	5.38	0.26	274.14	13.87
M2	9.04	0.93	288.15	42.57
M3	6.97	0.85	211.77	33.34
M4	7.3	0.46	236.24	13.6
M5	7.58	0.45	295.48	60.9
M6	9.81	0.91	249.09	38.13

## Chapter 4: Discussion

### I. Oxide particles characterization and size distribution

The oxide size distribution of the different samples is shown in Table 4.1. The interparticle distancing  $\lambda$  was calculated using the following equation [26]:

$$\lambda = \left[ \left( \frac{3\pi}{4f} \right)^{\frac{1}{2}} - 1.64 \right] r \quad (1)$$

Where  $f$  is the volume fraction of the oxides, and  $r$  is the mean particle radius. From this Table, the M5 sample has an average oxide particle size of 21.60 nm for both TEM images analyzed with 217 particle count, a number density of  $9.08 \times 10^{20}$  particle/m<sup>3</sup>, and a volume fraction of 0.75%. M3 samples have an average oxide particle size of 26.19 nm measured through two TEM images with a total particle count of 52, an average density of  $4.38 \times 10^{20}$  particle/ m<sup>3</sup>, and a volume fraction of 0.77%. The STEM-EDS maps of the M3 sample are shown in Figure 3.15. It's also evident from this image that the grains are enriched in Cr, suggesting segregation of Cr. The M4 sample showed the smallest oxide size of 18.815 nm and a volume fraction of 0.21%. The interparticle is lowest for the M5 with 180.24 nm, M3 had a particle distancing of 248.14, and M4 had an interparticle of 299.14.

Table 4.1: size distribution of the oxides made from the Cryo A samples.

Sample	Mag.	Average particle (nm)	D10 (nm)	D90 (nm)	D50 (nm)	Number density (# of particle/m <sup>3</sup> )	Volume fraction	Thickness (nm)	Particle count
M3	125 Kx	22.05	12.34	28.00	18.368	$3.38 \times 10^{20}$	0.618	197.90	42
	125 Kx	42.017	16.30	72.49	29.28	$9.11 \times 10^{19}$	0.9349	191.72	10
M4	32Kx	18.506	8.83	20.78	14.01	$2.59 \times 10^{20}$	0.211	123.93	157
M5	125 Kx	21.68	13.16	30.20	20.37	$9.40 \times 10^{20}$	0.8622	192.54	114
	125 Kx	21.49	13.36	32.39	19.52	$7.898 \times 10^{20}$	0.582	210.12	103

It appears from this image that the grains are enriched in Cr, suggesting segregation of Cr. M4 and M5 have less phase segregation. Although diffraction patterns of the M5 sample have provided valuable information about the D-spacing of an oxide, as shown in Figure 4.1. The D-spacing measurements of this oxide are provided in the Table 4.2. These values are very close to the D-spacings of  $Y_6ZrO_{11}$ , although these results need to be verified using HRTEM. The more considerable oxide shown in the TEM picture has an average oxide size of 45.25nm and  $Y_6ZrO_{11}$  tends to be larger as reported in [39]. The TEM image of Figure 4.1 shows two species of oxides, a minor oxide and a large one. The smaller one appears to be  $Y_4Zr_3O_{12}$  (PDF: 04-002-02, Rhombohedral structure) since it matches with  $(21\bar{5})$ ,  $(502)$ ,  $(14\bar{3})$ ,  $(42\bar{1})$ , and  $(404)$  with an error percentage ranging from 0.04% to 3.91% as shown in the table. This oxide has been shown to have much smaller sizes than  $Y_6ZrO_{11}$  and forms preferentially than other oxides due to its higher formation energy. Thus,  $Y_4Zr_3O_{12}$  is the main species formed and is smaller in size than other Y-Zr-O type oxides[39,40].

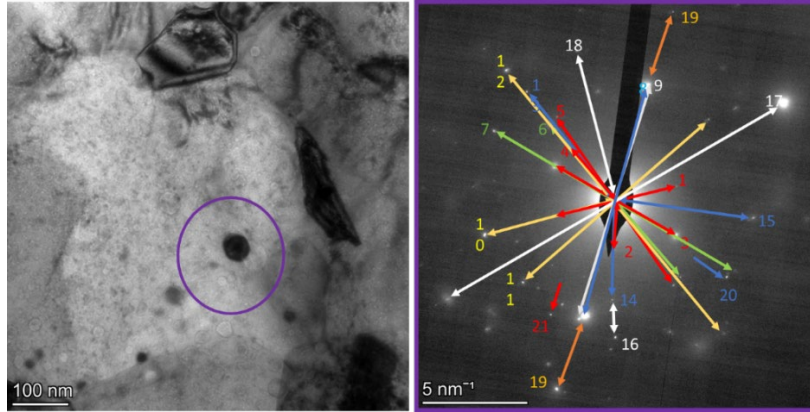


Figure 4.1: Selected area diffraction of M5 sample showing a potential  $Y_6ZrO_{11}$  and a  $Y_4Zr_3O_{12}$

Table 4.2: SAED of an oxide from the M5 sample indexation results.

Measured <i>d</i> -spacing	<i>d</i> (Å)	<i>h</i>	<i>K</i>	<i>l</i>	Error (%)	$Y_6ZrO_{11}$	Number
4.311	4.299	1	1	2	1.46	$Y_6ZrO_{11}$	2
3.327	3.355	1	1	4	-0.86	$Y_6ZrO_{11}$	1
3.023	3.059	1	0	6	1.35	$Y_6ZrO_{11}$	3
2.105	2.101	4	0	1	0.03	$Y_6ZrO_{11}$ or Ni	6
2.064	2.065	4	0	2	0.12	$Y_6ZrO_{11}$ or Ni	5
1.789	1.76	2	0	0	0.29	$Y_6ZrO_{11}$ or Ni	4
1.713	1.582	2	1	-5	0.04	$Y_4Zr_3O_{12}$	11
1.626	1.582	3	3	0	1.75	$Y_4Zr_3O_{12}$	21
1.558	1.574	2	1	-5	1.88	$Y_4Zr_3O_{12}$	20
1.554	1.569	4	2	-1	3.91	$Y_4Zr_3O_{12}$	10
1.554	1.547	4	0	4	2.50	$Y_4Zr_3O_{12}$	16
1.520	1.519	0	0	6	0	$Y_4Zr_3O_{12}$	15
1.516	1.519	0	0	6	-0.001	$Y_4Zr_3O_{12}$	7
1.504	1.504	2	4	-2	0	$Y_4Zr_3O_{12}$	13
1.24	1.26	2	2	0	-0.45	Ni	12
1.086	1.084	2	2	2	2.2	Ni	17
1.075	1.03	3	1	1	4.2	Ni	19

## II. Effect of the sintering parameters

TEM pictures of the different samples are shown in Figure 4.2. The TEM pictures show very small grains (nanosize) with a high fraction of twin boundaries in the case of the M4 and M5 samples which should explain the very high hardness measurement values in general. Table 4.3 shows the grain size of the different samples. For longer sintering times, the grains size increase as shown in Figure 4.3. Twin boundaries seem to be more active in the M4 and M5 samples. Twin boundary width is more significant in the M5 sample than in the M4 sample. This can be attributed to the bigger grain size of the M5 sample and the lower the grain boundary density[41].

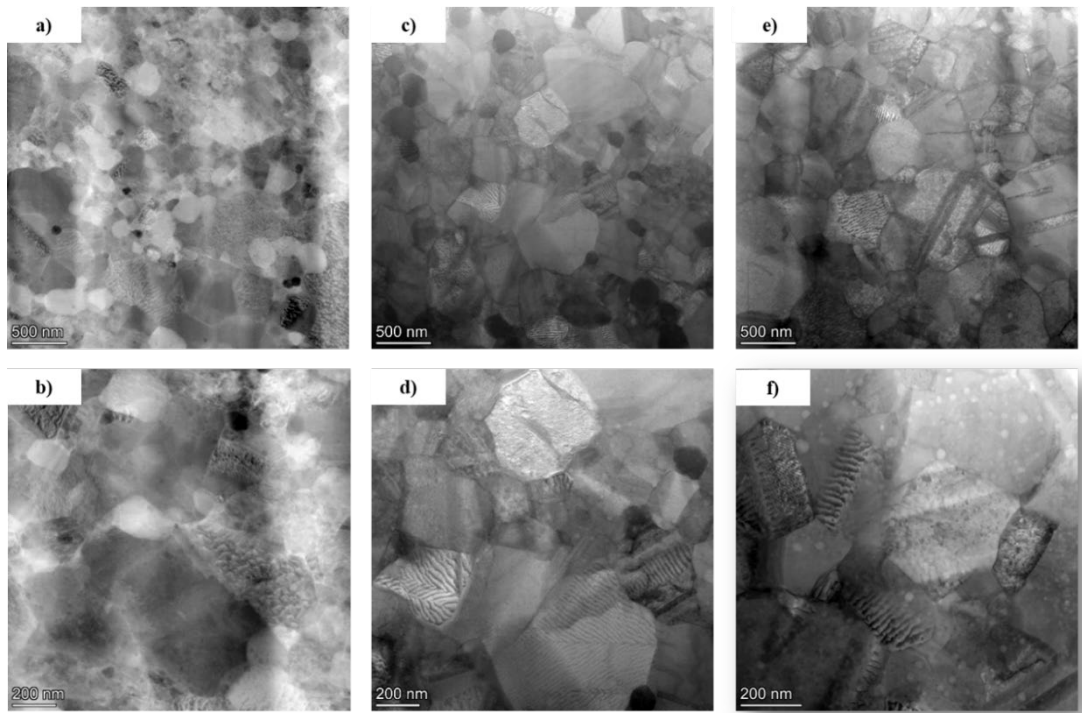


Figure 4.2: TEM pictures of a,b) M3 Sample, c,d) M4 sample, and e,f) M5 sample.

Table 4.3: Grain size of the different samples

Sample	Average Grain size			
	(nm)	D10 (nm)	D50(nm)	D90 (nm)
M2	144.47	65.76	124.66	254.67
M3	246.27	98.83	211.63	479.83
M4	300.74	153.72	246.75	536.64
M5	356.43	109.20	344.97	559.08
M6	151.35	88.27	162.28	279.07

The M5 sample has the largest average grain size, followed by M4 and M3. These results are expected since increasing the temperature leads to bigger grains. For M4, increasing the sintering duration from 2h to 6h increases the grain size.

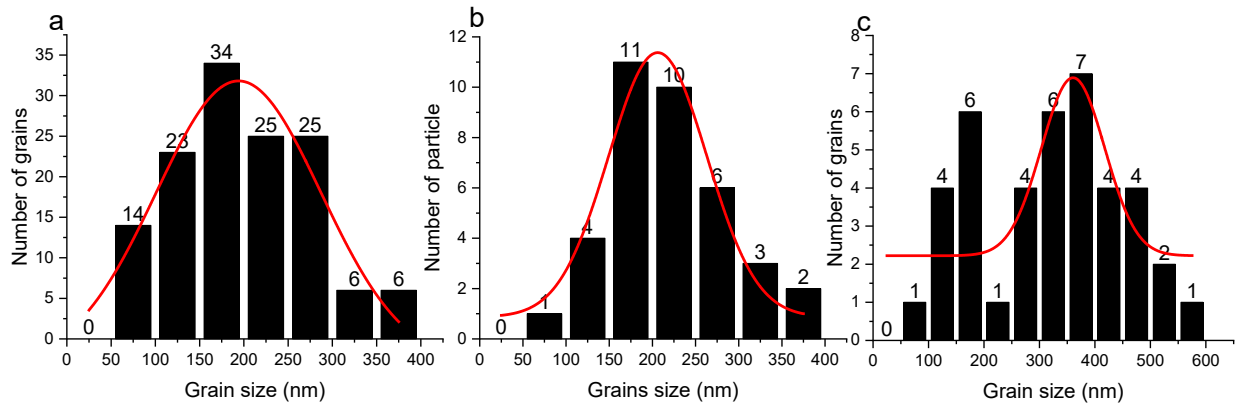


Figure 4.3: Grain size distribution: a) M3 sample, b) M4 sample, and c) M5 samples.

STEM-EDS maps of the different samples are shown in Figure 4.4.

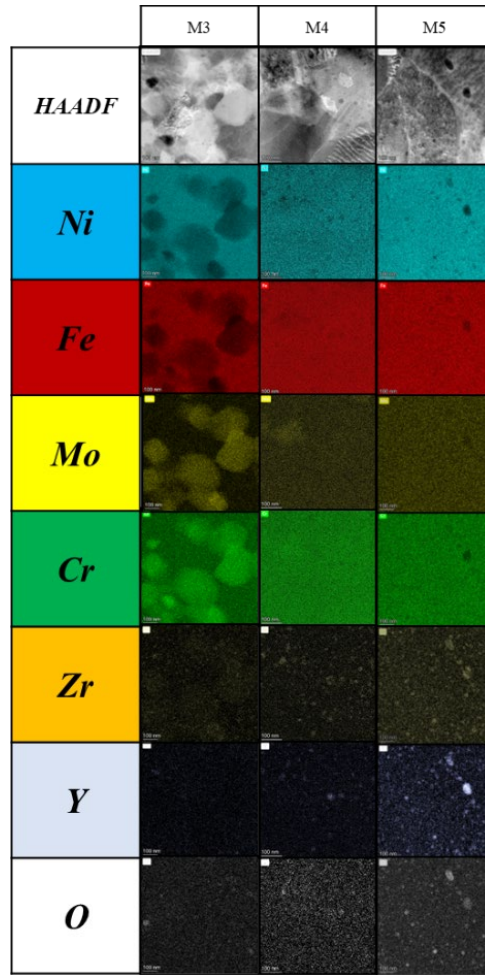


Figure 4.4: STEM-EDS map of the different consolidated samples made from the Cryo A powder.

M5, have the highest number density of oxides and minimal size distribution. M4 had a very small size distribution, with an average number density comparable to M3 of  $2.2 \times 10^{20}$  particles/m<sup>3</sup>. This suggests that a higher temperature annealing, and longer durations are more important to induce higher density of small oxides. This observation agrees with results found in the literature [42] which found that the most important factor is the annealing temperature and duration. The grains throughout the samples have slight variations in chemistries which may impact the phases present. M5 had a much smaller difference across grains in terms of elemental enrichment, suggesting that

treatment at 1125°C at longer durations is better than 1200°C for 2 hours. Unfortunately the 6 hour sintering at 1200C case was not available to check whether at 1200C the oxide population would be enhanced. This effect of oxide size refinement with higher temperature may be caused by forming a smaller size Y-Zr-O [43]. Higher sintering duration and pressure result in a higher alloy hardness value. Longer sintering duration resulted in the highest oxide density suggesting that the more the annealing duration, the more Y-Zr-O oxides form[42]. Hastelloy N derives its strength mainly from solid solution strengthening. However, various contribution affects the eventual final strength. Higher hardness could be attributed to the microstructure features through different strengthening mechanisms. Our results show that finer grains didn't correlate with higher strengthening for the Cryo A samples, which was supposed to be the case according to Hall-Petch[44]. Thus, considering other strengthening mechanisms; in general, the total strengthening  $\Delta\sigma_y$  can be due to the contribution of  $\sigma_0, \Delta\sigma_{ss}, \Delta\sigma_{GB}, \Delta\sigma_{Oro}, \Delta\sigma_c, \Delta\sigma_d$  where  $\sigma_y$  is the estimated yield strength,  $\sigma_0$  is the Peierls–Nabarro stress or lattice-friction stress and negligible,  $\Delta\sigma_{ss}$  is the solid solution strengthening contribution,  $\Delta\sigma_d$  is the dislocation strengthening contribution,  $\Delta\sigma_{GB}$  is the grain boundary strengthening contribution  $\Delta\sigma_{Oro}$  is the Orowan or dispersion mechanism contribution and  $\Delta\sigma_c$  is the composite strengthening contribution factor. The composite strengthening seems to be activated in the case of the M2 and M6 samples due to the presence of oxides and different phases other than the matrix. However, the higher hardness of M2 and M6 samples can be explained by the smaller size grains as well or a combination of the two.

M3, M4 and M5 samples are all made from Cryo A powder M5 had the smallest interparticle and a relatively small oxide size. The Orowan dispersion factor can be determined by the following

equation: 
$$\Delta\sigma_{Oro} = \frac{M0.4G}{\pi\sqrt{1-\nu}} \times \frac{\ln\frac{2r}{b}}{\lambda}$$

Where  $M=3$  for an FCC material,  $r$  average radius of the oxide particle,  $\lambda$  interparticle,  $b$  is the burger vector,  $G$  is shear stress,  $\nu$  is Poisson ratio. From the Orowan strengthening factor the higher oxide dispersion of the M5 sample could explain its higher hardness compared to M3 and M4 sample.

### **III.LPBF samples characterization**

#### **III.1 Samples density and effect of the powder**

The density of the pure Hastelloy N powder was estimated to be 8.90 g/cc after it was measured using the pycnometer. Cryo B density was estimated to be 8.59 g/cc. The density of the samples is summarized in Table 4.4. The samples manufactured with the highest volumetric energy seem to have a better density than the pure Hastelloy. 99% density was achieved with these samples for the hand blended and pure Hastelloy N samples. The primary issue for the samples made from cryo-milled powder is the flowability of the powder since, as seen in Figure 2.8, the particles have a flaky morphology and a size distribution that has been proven to be inadequate for the LPBF process. The hand-blended samples also appeared to have excellent density.

Table 4.4: Density of the different samples

<i>Sample</i>	<i>Powder</i>	<i>Sample weight (g)</i>	<i>Average Density (g/cm<sup>3</sup>)</i>
<i>P1</i>	Pure Hastelloy N	1.39	8.82
<i>P2</i>		1.40	8.76
<i>P3</i>		1.36	8.82
<i>P7</i>	Cryo-milled	1.01	8.06
<i>P8</i>		0.94	8.33
<i>P9</i>		0.93	8.11
<i>P10</i>	Blended	0.70	8.83
<i>P11</i>		0.56	8.71
<i>P12</i>		0.64	8.67

### III.2 Oxide size measurement of LPBF samples

Figure 4.5.c) shows STEM-EDS maps of LPBF samples. The P6 sample has an average particle size of 44.36 nm, with a number density of  $2.95 \times 10^{19}$  particle /m<sup>3</sup> and a volume fraction of 0.22%; the interparticle separation was determined to be 246.63 nm. The P9 sample had an average particle size of 49.01 nm, a number density of  $1.33 \times 10^{20}$ , a volume fraction of 1.23%, and an interparticle of 376.11 nm. P12 had an average particle size of 21.49 nm, a number density of  $2.42 \times 10^{20}$ , a volume fraction of 0.21 %, and an interparticle of 57.96 nm. These results are summarized in Table 4.5.

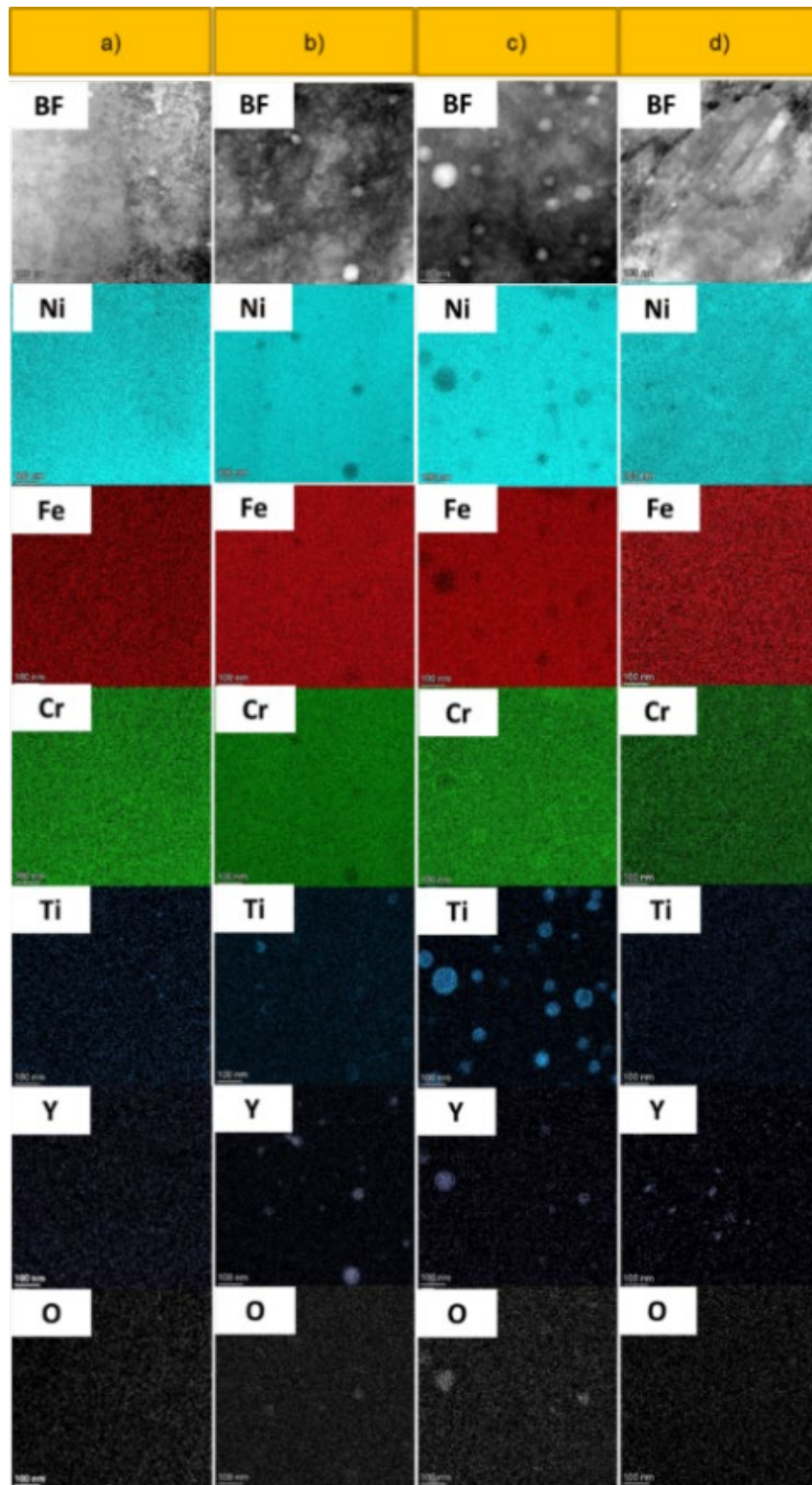


Figure 4.5: STEM-EDS images of column a) P3 b) P6 c) P9 d) P12.

Table 4.5: oxide size measurement and distribution.

<i>Sample</i>	<i>Average size (nm)</i>	<i>D10(nm)</i>	<i>D50(nm)</i>	<i>D90(nm)</i>	<i>Number density (particle/m<sup>3</sup>)</i>	<i>Volume fraction (%)</i>	<i>Interparticle (nm)</i>	<i>Particle Count</i>
<i>P6</i>	44.36	20.91	44.08	70.8	2.95E+19	0.22	123.32	30
<i>P9</i>	49.01	29.94	45.44	69.04	1.33E+20	1.23	376.11	123
<i>P12</i>	21.49	10.29	19.05	34.88	2.42E+20	0.21	57.96	108

### III.5 Comparison between LPBF and sintering

The oxide size measurement for the LPBF samples have shown That the p-samples have similar oxide density to their counterparts made with sintering. Core shell structure was observed for samples made from cryo B In LPBF as shown in chapter 3 and their chemical composition have been shown to be different. However, for Cryo B sintered samples this has not been seen. Although the condition of the sintering seems not to be optimal so no clear conclusion can be drawn for now. Table 4.6 shows the oxide measurement for both samples.

Table 4.6: Comparison of Cryo B AM samples and Cryo B sintered sample.

Sample	Mag	Average effective size	D10	D50	D90	Number density (particles/m <sup>3</sup> )	Volume percent	Thickness (nm)	Particle count
P9	45 Kx	47.88	28.98	64.7	44.88	1.27×10 <sup>20</sup>	1.13	160.94	101
	125 Kx	53.53	38.96	68.99	50.01	1.631×10 <sup>20</sup>	1.77	215.67	24
M6	45 Kx	46.92	31.21	88.91	43.67	1.104×10 <sup>20</sup>	1.25	93.744	52
	125 Kx	39.53	15.43	79.06	24.64	1.107×10 <sup>20</sup>	1.03	143.35	10

## Summary and Conclusions

Hastelloy N powder was used to develop a Ni-based ODS alloys with different additions of  $Y_2O_3$  and Ti or Zr.

Different sintering and annealing parameters were used to produce the M samples. Most of the sintered sample showed some elemental segregation. Thus, heat treatment should be the next phase to optimize these samples. M5 showed a good oxide density and small oxides around 21.5 nm in size indicating adequate consolidation conditions and that higher temperature annealing and longer duration leads to smaller oxide size. Overall, 2200 psi sintering followed by annealing for 6 hours at 1125°C showed a desired microstructure: high twinning ratio and much better phase homogeneity and a desired oxide distribution. Sample M4 was also decent and very similar to M5 and even had smaller average oxide size.

Hardness is much higher for the samples made with Ti addition. This can be explained by the smaller grains in this samples and this is due to the ability to of Y-Ti-O to inhibit grain growth more efficiently than Y-Zr-O. Also, these samples showed phase segregation which correlate to increased strengthening. The samples made from Cryo A showed increase of hardness when increasing the sintering pressure. Bigger grain size didn't correlate to higher strengthening this might be due to that smaller oxide and higher volume fraction has a big impact on the strength. Annealing temperature and duration is the most crucial factor that affect the oxide size and density. The oxides nature was investigated for the samples, and it was found to be dominantly  $Y_4Zr_3O_{12}$ , but this needs to be confirmed using HRTEM.

LPBF was used to consolidate samples and 99.21% density of the pure Hastelloy N sample was achieved and similarly for the hand-blended powder. This results also emphasis that these samples

don't need any supplementary heat treatment due to the higher cooling rates of the LPBF process. In contrast, to the sintering processing. The LPBF have shown an elongated grain structure that grows along the direction of building etching revealed overlapped melt pools that forms the grains. In terms of oxide dispersion LPBF had similar oxide distribution. Core/shell structure of the oxides is observed indicating that LPBF conditions facilitate the formation of the Cr shell.

Hardness testing of the LPBF samples can provide us a good comparison with the sintered samples. HRTEM can confirm the nature of the oxides. Future irradiation experiments and composition/process optimization will provide us the complete image of the capabilities of our alloy in terms of irradiation resistance since, molten salt corrosion resistance of Hastelloy N have been proven to be adequate for Molten salt reactor structural applications.

## References

- [1] S.S. Raiman, D. Sulejmanovic, J.M. Kurley, J. Lee, C.G. Parker, B.A. Pint, TECHNICAL ASSESSMENT OF MATERIALS COMPATIBILITY IN MOLTEN SALT REACTORS March 2021 PREPARED FOR: U.S. Nuclear Regulatory Commission TASK ORDER NO. 3131002N0007 (Task 1) PREPARED BY: Oak Ridge National Laboratory, n.d.
- [2] G.R. Odette, Recent Progress in Developing and Qualifying Nanostructured Ferritic Alloys for Advanced Fission and Fusion Applications, JOM. 66 (2014) 2427–2441. <https://doi.org/10.1007/s11837-014-1207-5>.
- [3] G.R. Odette, M.J. Alinger, B.D. Wirth, Recent developments in irradiation-resistant steels, Annu Rev Mater Res. 38 (2008) 471–503. <https://doi.org/10.1146/annurev.matsci.38.060407.130315>.
- [4] H.K.D.H. Bhadeshia, A Recrystallisation of practical mechanically alloyed iron-base and nickel-base superalloys, 1997.
- [5] S.J. Zinkle, N.M. Ghoniem, Operating temperature windows for fusion reactor structural materials, 2000. [www.elsevier.com/locate/fusengdes](http://www.elsevier.com/locate/fusengdes).
- [6] H.E. McCoy, O A K RIDGE N A T I O N A L LABORATORY operated by UNION CARBIDE CORPORATION NUCLEAR DIVISION A N EVALUATION OF THE MOLTEN SALT REACTOR EXPERIMENT HASTELLOY N SURVEILLANCE SPECIMENS-FIRST GROUP, n.d.
- [7] W. Cao, S. Xia, Q. Bai, W. Zhang, B. Zhou, Z. Li, L. Jiang, Effects of initial microstructure on the grain boundary network during grain boundary engineering in Hastelloy N alloy, J Alloys Compd. 704 (2017) 724–733. <https://doi.org/10.1016/j.jallcom.2017.02.009>.

- [8] R.E. Gehlbach, H.E. McCoy, PHASE INSTABILITY IN HASTELLOY N, n.d.
- [9] J. Gao, L. Bao, H. Huang, Y. Li, Q. Lei, Q. Deng, Z. Liu, G. Yang, L. Shi, ERDA, RBS, TEM and SEM characterization of microstructural evolution in helium-implanted Hastelloy N alloy, *Nucl Instrum Methods Phys Res B.* 399 (2017) 62–68. <https://doi.org/10.1016/j.nimb.2017.03.148>.
- [10] A. García-Junceda, E. Macía, D. Garbiec, M. Serrano, J.M. Torralba, M. Campos, Effect of small variations in Zr content on the microstructure and properties of ferritic ODS steels consolidated by SPS, *Metals (Basel)*. 10 (2020). <https://doi.org/10.3390/met10030348>.
- [11] K.R. Rao, S.K. Sinha, Effect of sintering temperature on microstructural and mechanical properties of SPS processed CoCrCuFeNi based ODS high entropy alloy, *Mater Chem Phys.* 256 (2020). <https://doi.org/10.1016/j.matchemphys.2020.123709>.
- [12] H. Zhang, Y. Huang, H. Ning, C.A. Williams, A.J. London, K. Dawson, Z. Hong, M.J. Gorley, C.R.M. Grovenor, G.J. Tatlock, S.G. Roberts, M.J. Reece, H. Yan, P.S. Grant, Processing and microstructure characterisation of oxide dispersion strengthened Fe-14Cr-0.4Ti-0.25Y<sub>2</sub>O<sub>3</sub> ferritic steels fabricated by spark plasma sintering, *Journal of Nuclear Materials.* 464 (2015) 61–68. <https://doi.org/10.1016/j.jnucmat.2015.04.029>.
- [13] H. Xu, Z. Lu, D. Wang, C. Liu, Effect of zirconium addition on the microstructure and mechanical properties of 15Cr-ODS ferritic Steels consolidated by hot isostatic pressing, *Fusion Engineering and Design.* 114 (2017) 33–39. <https://doi.org/10.1016/j.fusengdes.2016.11.011>.
- [14] I. Hilger, X. Boulnat, J. Hoffmann, C. Testani, F. Bergner, Y. de Carlan, F. Ferraro, A. Ulbricht, Fabrication and characterization of oxide dispersion strengthened (ODS) 14Cr

- steels consolidated by means of hot isostatic pressing, hot extrusion and spark plasma sintering, *Journal of Nuclear Materials*. 472 (2016) 206–214. <https://doi.org/10.1016/j.jnucmat.2015.09.036>.
- [15] W. He, F. Liu, L. Tan, L. Huang, Y. Nie, G. Wang, X. Zhan, Z. Qin, Bimodal-grained high-strength nickel-base ODS alloy fabricated by mechanical alloying and hot extrusion, *Mater Today Commun*. 26 (2021). <https://doi.org/10.1016/j.mtcomm.2020.101921>.
- [16] J. Zbiral, *Tensile Properties of Mechanically Alloyed/Milled ODS-Ni-Based Alloys*, n.d.
- [17] S. Pasebani, A.K. Dutt, J. Burns, I. Charit, R.S. Mishra, Oxide dispersion strengthened nickel based alloys via spark plasma sintering, *Materials Science and Engineering A*. 630 (2015) 155–169. <https://doi.org/10.1016/j.msea.2015.01.066>.
- [18] M. Sivakumar, A. Dasgupta, C. Ghosh, D. Sornadurai, S. Saroja, Optimisation of high energy ball milling parameters to synthesize oxide dispersion strengthened Alloy 617 powder and its characterization, *Advanced Powder Technology*. 30 (2019) 2320–2329. <https://doi.org/10.1016/j.appt.2019.07.014>.
- [19] C. Suryanarayana, *Mechanical alloying and milling*, 2001. [www.elsevier.com/locate/pmatsci](http://www.elsevier.com/locate/pmatsci).
- [20] [www.retsch.com](http://www.retsch.com), An expert guide to neutral-to-analysis size reduction and homogenization in the laboratory *The Art of Milling 2*, 2017.
- [21] C. Kim, J. Yoon, J. Lim, J. Park, Microstructures and mechanical properties of TiO<sub>2</sub> dispersion strengthened nickel prepared using an alloying-carbonizing-oxidation-sintering process, *J Alloys Compd*. 791 (2019) 87–95. <https://doi.org/10.1016/j.jallcom.2019.03.223>.

- [22] H.E. Lee, Y.S. Kim, J.K. Park, S.T. Oh, Microstructure Evolution of Ni-Based ODS Superalloy Powders during Horizontal Rotary Ball Milling, *Archives of Metallurgy and Materials*. 62 (2017) 1253–1255. <https://doi.org/10.1515/amm-2017-0187>.
- [23] J. Jang, T.K. Kim, C.H. Han, H.K. Min, S.H. Jeong, D.H. Kim, A preliminary development and characterization of Ni-based ODS alloys, in: *Procedia Eng*, Elsevier Ltd, 2013: pp. 284–288. <https://doi.org/10.1016/j.proeng.2013.03.255>.
- [24] J. Park, J. Jang, T.K. Kim, S.-J. Kim, J.-H. Ahn, Formation of nanostructures in Ni-22Cr-11Fe-1X (X = Y<sub>2</sub>O<sub>3</sub>, TiO<sub>2</sub>) alloys by high-energy ball-milling, *J Nanosci Nanotechnol*. 11 (2011) 6213–6218. <https://doi.org/10.1166/jnn.2011.4411>.
- [25] M. Magini, F. Padella, 0956-716X(95)00465-3 BALL MILLING: AN EXPERIMENTAL SUPPORT TO THE ENERGY TRANSFER EVALUATED BY THE COLLISION MODEL, *Acta Metallurgica Inc*, 1996.
- [26] S. Pasebani, A.K. Dutt, J. Burns, I. Charit, R.S. Mishra, Oxide dispersion strengthened nickel based alloys via spark plasma sintering, *Materials Science and Engineering A*. 630 (2015) 155–169. <https://doi.org/10.1016/j.msea.2015.01.066>.
- [27] J. Stubbins, A. Gewirth, B. Heuser, I. Robertson, H. Sehitoglu, P. Sofronis, S. Supported Aaron Oaks, D. Gross, X. Han, X. Liu, Y. Miao, J. Sanders, Development of Austenitic ODS Strengthened Alloys for Very High Temperature Applications *Nuclear Energy Enabling Technologies*, 2011.
- [28] H. Oka, M. Watanabe, N. Hashimoto, S. Ohnuki, S. Yamashita, S. Ohtsuka, Morphology of oxide particles in ODS austenitic stainless steel, *Journal of Nuclear Materials*. 442 (2013) S164–S168. <https://doi.org/10.1016/j.jnucmat.2013.04.073>.

- [29] X. Mao, K.H. Oh, S.H. Kang, T.K. Kim, J. Jang, On the coherency of Y<sub>2</sub>Ti<sub>2</sub>O<sub>7</sub> particles with austenitic matrix of oxide dispersion strengthened steel, *Acta Mater.* 89 (2015) 141–152. <https://doi.org/10.1016/j.actamat.2015.01.060>.
- [30] N. Oono, Q.X. Tang, S. Ukai, Oxide particle refinement in Ni-based ODS alloy, *Materials Science and Engineering A.* 649 (2016) 250–253. <https://doi.org/10.1016/j.msea.2015.09.094>.
- [31] C.W. Park, J.M. Byun, W.J. Choi, S.Y. Lee, Y. do Kim, Improvement of high temperature mechanical properties of Ni-based oxide dispersion strengthened alloys by preferential formation of Y-Ti-O complex oxide, *Materials Science and Engineering A.* 740–741 (2019) 363–367. <https://doi.org/10.1016/j.msea.2018.10.004>.
- [32] S. Ohtsuka, S. Ukai, M. Fujiwara, T. Kaito, T. Narita, Nano-structure control in ODS martensitic steels by means of selecting titanium and oxygen contents, in: *Journal of Physics and Chemistry of Solids*, 2005: pp. 571–575. <https://doi.org/10.1016/j.jpcs.2004.06.033>.
- [33] C. Capdevila, H.K.D.H. Bhadeshia, Manufacturing and microstructural evolution of mechanically alloyed oxide dispersion strengthened superalloys, *Adv Eng Mater.* 3 (2001) 647–656. [https://doi.org/10.1002/1527-2648\(200109\)3:9<647::AID-ADEM647>3.0.CO;2-4](https://doi.org/10.1002/1527-2648(200109)3:9<647::AID-ADEM647>3.0.CO;2-4).
- [34] J. Jang, T.K. Kim, C.H. Han, H.K. Min, S.H. Jeong, D.H. Kim, A preliminary development and characterization of Ni-based ODS alloys, in: *Procedia Eng*, Elsevier Ltd, 2013: pp. 284–288. <https://doi.org/10.1016/j.proeng.2013.03.255>.
- [35] J. Zbiral, G. Jangg, H.J. Ullrich, G. Korb, H. Oettel, INFLUENCE OF PROCESSING PARAMETERS ON THE SUBSTRUCTURE OF ODS ALLOYS, n.d.

- [36] M. Wang, H.N. Han, H.S. Chung, Y.B. Chun, J. Jang, In situ observation of nanoparticle formation in nickel-based mechanical alloyed powders, *J Mater Sci.* 53 (2018) 16110–16121. <https://doi.org/10.1007/s10853-018-2761-y>.
- [37] L. Raman, K. Gothandapani, B.S. Murty, Austenitic oxide dispersion strengthened steels: A review, *Def Sci J.* 66 (2016) 316–322. <https://doi.org/10.14429/dsj.66.10205>.
- [38] W. Li, T. Hao, R. Gao, X. Wang, T. Zhang, Q. Fang, C. Liu, The effect of Zr, Ti addition on the particle size and microstructure evolution of yttria nanoparticle in ODS steel, *Powder Technol.* 319 (2017) 172–182. <https://doi.org/10.1016/j.powtec.2017.06.041>.
- [39] S. Cao, Z. Zhou, Microstructure and mechanical properties of an ODS ferritic steel with very low Cr content, *Journal of Nuclear Materials.* 551 (2021). <https://doi.org/10.1016/j.jnucmat.2021.152971>.
- [40] L. Yu, Z. Lu, S. Peng, X. Li, Effects of hot rolling and annealing temperature on microstructure and tensile properties of a Zr-containing Ni-based ODS superalloy, *J Alloys Compd.* 918 (2022). <https://doi.org/10.1016/j.jallcom.2022.165625>.
- [41] D. Horton, C.B. Thomson, V. Randle, *Aspects of twinning and grain growth in high purity and commercially pure nickel*, 1995.
- [42] R. Gao, T. Zhang, H.L. Ding, Y. Jiang, X.P. Wang, Q.F. Fang, C.S. Liu, Annealing effects on the microstructure and mechanical properties of hot-rolled 14Cr-ODS steel, *Journal of Nuclear Materials.* 465 (2015) 268–279. <https://doi.org/10.1016/j.jnucmat.2015.05.038>.

- [43] H. Lu, C. Zhang, J. Xu, G. Xu, Y. Zhang, J. Suo, Effects of N addition and annealing treatment on microstructures and mechanical properties of ODS steels, *Journal of Nuclear Materials*. 527 (2019). <https://doi.org/10.1016/j.jnucmat.2019.151796>.
- [44] A. Melander, B. Jansson, The Strength of Dispersion and Precipitation Hardened Alloys, in: P. HAASEN, V. GEROLD, G. KOSTORZ (Eds.), *Strength of Metals and Alloys*, Pergamon, 1979: pp. 627–632. <https://doi.org/https://doi.org/10.1016/B978-1-4832-8412-5.50107-7>.